Check for updates

EcoEnergy

WILEY

EcoEnergy Open Access

REVIEW OPEN ACCESS

Synergistic Optical Strategies for Enhanced Perovskite Photocatalytic Activity

Jaemin Jeong[1] | Myeongjin Seol[1] | Sang Hyun Ahn[2] | Soo Young Kim[1]

[1]Department of Materials Science and Engineering, Korea University, Seoul, Republic of Korea | [2]Department of Chemical Engineering, Chung-Ang University, Seoul, Republic of Korea

Correspondence: Sang Hyun Ahn (shahn@cau.ac.kr) | Soo Young Kim (sooyoungkim@korea.ac.kr)

Received: 13 March 2026 | **Revised:** 7 May 2026 | **Accepted:** 28 May 2026

Keywords: halide perovskite | optical engineering | photocatalytic CO_2 reduction | photonic crystals | plasmonic enhancement

ABSTRACT

Photocatalysis is a key pathway for solar-to-chemical conversion, enabling the production of sustainable fuels and value-added chemicals. Halide perovskites have attracted increasing attention as photocatalysts or photoactive components due to their strong visible-light absorption, composition-tunable bandgaps, and favorable optoelectronic properties. However, practical performance is often limited by optical losses, charge recombination, and inefficient interfacial charge transfer. This review addresses these bottlenecks from an optics-driven perspective and organizes recent advances into four interconnected design principles: electronic structure engineering, interfacial design for photocarrier separation and band alignment, structural optical and spin-selective engineering, and plasmonic metal–semiconductor synergy. By connecting photon management with charge kinetics and interfacial reactivity, this review provides practical design principles and outlines key directions toward efficient, selective, and stable perovskite photocatalysis for CO_2 reduction.

1 | Introduction

The rapid increase in fossil fuel consumption since industrialization has not only led to the depletion of energy resources but also caused a sharp rise in atmospheric carbon dioxide concentrations, triggering a global climate crisis. To fundamentally address these issues, artificial photosynthesis is garnering significant attention as a sustainable energy solution that mimics natural photosynthesis to convert CO_2 into high-value chemical fuels such as CO [1–6], CH_4 [7–10], and HCOOH [11–13] using inexhaustible solar energy. Over the past decades, metal oxide-based photocatalysts such as TiO_2 and ZnO have been extensively studied [14–19]. However, their wide bandgaps limit their absorption to the ultraviolet (UV) spectrum, which accounts for only 4% of total sunlight, posing a fundamental constraint on utilizing the full solar spectrum. Consequently, it is essential to develop next-generation photocatalytic materials capable of efficiently absorbing the visible-light region, which constitutes the majority of solar energy, while maintaining high charge separation efficiency.

Recently, metal halide perovskites (MHPs) have rapidly emerged as promising materials in the field of photocatalysis, building on their remarkable success in photovoltaics [20–23]. Compared to conventional inorganic semiconductors, perovskites exhibit exceptional optoelectronic properties, including high absorption coefficients, long charge-carrier diffusion lengths, and low exciton binding energies [24, 25]. In particular, their tunable bandgap, achieved through the substitution or mixing of ions at the A, B, and X sites, offers a unique opportunity for maximizing visible-light absorption efficiency [26, 27]. These intrinsic characteristics allow MHPs to absorb a broad spectrum of light while

This is an open access article under the terms of the Creative Commons Attribution License, which permits use, distribution and reproduction in any medium, provided the original work is properly cited.

© 2026 The Author(s). *EcoEnergy* published by John Wiley & Sons Australia, Ltd on behalf of China Chemical Safety Association.

maintaining sufficient redox potential required for driving effective CO_2 reduction reactions.

Despite this inherent potential, the practical implementation of perovskite-based photocatalysis is still hindered by several critical challenges. In addition to stability concerns, such as sensitivity to moisture and polar solvents [28, 29], optical losses can also contribute to limitations in overall catalytic efficiency. Conventional structures, typically in the form of simple powders or thin films, often suffer from surface reflection, insufficient light scattering, and short optical path lengths [30], leading to incomplete light harvesting. In addition, defect-assisted recombination and inefficient interfacial charge transfer can further limit the utilization of photogenerated carriers in surface redox reactions. Consequently, bandgap tuning alone is insufficient, and improvements in both charge-management and optical engineering strategies are required to achieve efficient photocatalysis [31].

Several valuable review articles have summarized the rapid development of halide perovskite photocatalysts from broad material- and application-oriented perspectives, covering topics such as compositional design, heterojunction construction, cocatalyst integration, and stability improvement across various photocatalytic reactions. However, a perspective that systematically reorganizes these advances through an optics-driven framework remains relatively limited. In particular, the interconnected roles of bandgap tuning, structural light management, and plasmon-assisted processes have not been sufficiently discussed in a unified manner in relation to photon utilization, charge-carrier dynamics, and interfacial redox requirements for CO_2 photoreduction. Therefore, rather than providing another general survey of perovskite photocatalysis, this review specifically focuses on how optical engineering strategies can be used to improve the performance of halide perovskite photocatalysts for CO_2 reduction.

In this review, we comprehensively address the latest optical design strategies aimed at enhancing the CO_2 reduction performance of halide perovskite-based photocatalysts (Figure 1). We first introduce the fundamental requirements for CO_2 photoreduction. We then organize recent advances into four interconnected design strategies: electronic structure design for light absorption and redox driving force, interfacial design for charge separation and band alignment, structural optical design for enhanced photon utilization, and plasmonic enhancement through near-field effects, hot-electron injection, and plasmonic mediation. Finally, we summarize comparative design rules and discuss unresolved challenges for future perovskite photocatalyst development.

2 | Fundamentals of Photocatalysis and Optical Properties in Perovskites

Photocatalytic CO_2 reduction is a representative solar-to-chemical conversion process in which photogenerated carriers are used to transform thermodynamically stable CO_2 molecules into energy-rich carbon products. In halide perovskite-based

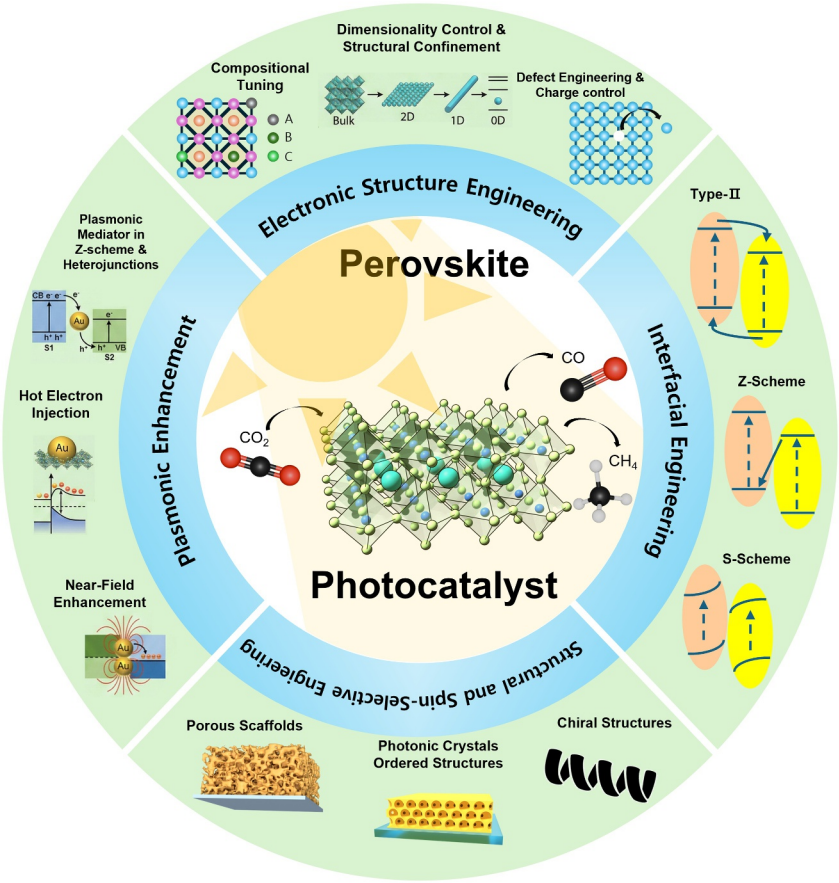


FIGURE 1 | Schematic overview of optics-driven engineering strategies for enhancing halide perovskite photocatalysts for CO_2 reduction.

28359399, 0, Downloaded from https://onlinelibrary.wiley.com/doi/10.1002/ece2.70090 by Chung-Ang University, Wiley Online Library on [02/08/2026]. See the Terms and Conditions (https://onlinelibrary.wiley.com/terms-and-conditions) on Wiley Online Library for rules of use; OA articles are governed by the applicable Creative Commons License

systems, this process is governed not only by intrinsic optical absorption but also by subsequent charge separation dynamics, interfacial charge transfer, and surface reaction kinetics. Therefore, a fundamental understanding of semiconductor photocatalysis and the unique optoelectronic properties of halide perovskites is required before discussing specific engineering strategies. This section first summarizes the general mechanism of semiconductor photocatalysis and then discusses the reaction pathways and product selectivity of CO_2 photoreduction.

2.1 | General Mechanism of Semiconductor Photocatalysis

The photocatalytic process involves utilizing solar energy to generate charge carriers within a semiconductor material, which subsequently migrate to the surface to drive chemical redox reactions. Regardless of whether the target application is CO_2 reduction or hydrogen evolution, all semiconductor-based photocatalytic systems follow three fundamental steps [32].

Step 1 Photoexcitation and charge-carrier generation

When a semiconductor absorbs a photon with energy equal to or greater than its bandgap energy ($h\nu \geq E_g$), an electron in the valence band (VB) is excited to the conduction band (CB). This excitation process generates a pair of an electron (e^-) and a hole (h^+).

$$\text{Semiconductor} + h\nu \rightarrow e^-_{CB} + h^+_{VB}$$

Step 2 Charge-carrier dynamics

The generated electrons and holes either bind as excitons through coulombic attraction or dissociate into free carriers [33]. Once separated, these charges migrate toward surface active sites through diffusion driven by concentration gradients or an internal electric field. The most critical loss factor during this stage is recombination. Recombination caused by defects is categorized into two types: bulk recombination, where electrons and holes recombine at internal defects or grain boundaries within the crystal, and surface recombination, where charges are captured and neutralized by surface trap states [34].

Step 3 Surface redox reaction

Upon reaching the surface, the charge carriers undergo electron transfer with adsorbed reactants to initiate chemical reactions, whose thermodynamic spontaneity is governed by the relative alignment of the band edges. Specifically, the conduction-band potential (E_{CB}) must be more negative than the reduction potential of the target species (E_{red}) to facilitate reduction, whereas the valence-band potential (E_{VB}) must be more positive than the relevant oxidation potential (E_{ox}) to drive the corresponding oxidation reaction [35].

2.2 | Reaction Pathways and Product Selectivity

Photocatalytic CO_2 reduction proceeds through a series of surface adsorption, activation, proton-coupled electron-transfer, and product-desorption steps. Because CO_2 has a stable linear O=C=O structure, its activation generally requires electron transfer accompanied by structural bending of the molecule. In practical photocatalytic systems, CO_2 reduction usually occurs through adsorbed reaction intermediates rather than direct one-step conversion. The final product is determined by how strongly these intermediates bind to the catalytic surface and how efficiently photogenerated electrons and protons are supplied. In general, the conduction-band minimum should be sufficiently negative to drive CO_2 reduction, whereas the valence-band maximum should be positive enough to support hole-consuming oxidation reactions, such as water oxidation or sacrificial-agent oxidation.

Among the possible CO_2 reduction products, CO is one of the most common products because it requires only a two-electron reduction process.

$$CO_2 + 2H^+ + 2e^- \rightarrow CO + H_2O$$

The CO formation pathway generally involves the generation of an adsorbed *COOH intermediate, followed by its reduction to *CO. When the binding strength of *CO is moderate, *CO readily desorbs from the surface as CO. Therefore, CO-selective photocatalysis requires active sites that can stabilize *COOH while avoiding excessive *CO binding. If *CO binds too weakly, CO_2 activation becomes inefficient, and if it binds too strongly, further hydrogenation or surface poisoning may occur.

In contrast, CH_4 formation requires a deeper eight-electron reduction process.

$$CO_2 + 8H^+ + 8e^- \rightarrow CH_4 + 2H_2O$$

Unlike CO formation, CH_4 production requires the continuous hydrogenation of *CO-derived intermediates. After *CO is formed, it must remain adsorbed on the catalyst surface and undergo successive proton-coupled electron-transfer steps through intermediates such as *CHO, *CH_2O, *OCH_3, or *CH_3 before final CH_4 desorption. Therefore, CH_4 formation is kinetically more demanding than CO formation because it requires multiple electrons and protons to be accumulated at the same active site while suppressing charge recombination and premature *CO desorption.

More complex reduction pathways can lead to C_2 products such as C_2H_4 and C_2H_6. These products require not only multi-electron transfer but also C–C coupling between carbon-containing intermediates.

$$2CO_2 + 12H^+ + 12e^2 \rightarrow C_2H_4 + 4H_2O$$
$$2CO_2 + 14H^+ + 14e^- \rightarrow C_2H_6 + 4H_2O$$

The formation of C_2 products generally proceeds through the coupling of adsorbed C1 intermediates, particularly *CO or hydrogenated *CO species. For this reason, the catalyst surface must provide active sites that can retain *CO long enough to enable C–C bond formation while also supplying sufficient electrons and protons for subsequent hydrogenation. This requirement makes C_2 product formation much more challenging than CO or CH_4 generation. In particular, metal sites such as Cu are often considered favorable for C–C coupling because they can bind *CO with appropriate strength and promote the formation of coupled intermediates.

28359399, 0, Downloaded from https://onlinelibrary.wiley.com/doi/10.1002/ece2.70090 by Chung-Ang University, Wiley Online Library on [02/08/2026]. See the Terms and Conditions (https://onlinelibrary.wiley.com/terms-and-conditions) on Wiley Online Library for rules of use; OA articles are governed by the applicable Creative Commons License

Overall, the product selectivity of CO_2 photoreduction is governed by the balance among intermediate adsorption, electron/proton supply, and product desorption. CO formation is favored when *COOH formation and *CO desorption are efficient. CH_4 formation requires stronger retention and stepwise hydrogenation of *CO-derived intermediates. C_2H_4 and C_2H_6 formation further requires C–C coupling between adsorbed carbon intermediates. Therefore, selective CO_2 photoreduction cannot be achieved by light absorption alone; it requires coordinated control of charge separation, surface active sites, and intermediate binding strength.

2.3 | Intrinsic Advantages of Halide Perovskites

Compared to traditional metal oxide photocatalysts such as TiO_2 and ZnO, halide perovskites offer significant photophysical advantages across the three fundamental stages of photocatalysis described above. First, as direct-bandgap semiconductors, perovskites exhibit a steep absorption edge that allows photon absorption without requiring phonon assistance [36]. This characteristic results in a sharp increase in the absorption coefficient near the bandgap, ensuring high photogenerated-carrier densities even within thin active layers. Furthermore, the tunable bandgap engineering of perovskites provides remarkable flexibility in material design. By adjusting the halide ratios at the X site [37–39] or substituting cations at the A [40–42] and B [43, 44] sites, the bandgap can be systematically tuned to optimize solar spectrum harvesting and precisely align the band-edge positions with the specific redox potentials of the target reaction. In terms of charge-carrier dynamics, perovskites are characterized by ambipolar transport and long diffusion lengths [45, 46]. The balanced effective masses of electrons and holes contribute to superior mobility for both carriers, whereas the low exciton binding energy facilitates easy dissociation into free charges [47]. These factors collectively enable diffusion lengths on the order of several micrometers, significantly increasing the probability that charge carriers will reach surface active sites before undergoing recombination.

2.4 | Theoretical Fundamentals of Optical Engineering

Despite the intrinsic optoelectronic advantages of halide perovskites, a considerable gap persists between their theoretical potential and the actual efficiencies achieved in practical photocatalytic systems. This gap arises from coupled losses in photon harvesting, charge separation, interfacial charge transfer, and surface redox reactions. The overall photocatalytic efficiency (η_{total}) is fundamentally determined by the product of three critical factors: light absorption efficiency (η_{abs}), charge separation efficiency (η_{cs}), and surface reaction efficiency (η_{sr}), which can be expressed in the following equation [48]:

$$\eta_{\text{total}} = \eta_{\text{abs}} \times \eta_{\text{cs}} \times \eta_{\text{sr}}$$

Although material synthesis, defect passivation, and interfacial engineering can improve charge separation and surface reaction kinetics, they do not fully resolve photon-management losses such as reflection, weak light trapping, and incomplete absorption. Therefore, optical engineering serves as a complementary strategy to increase usable photogenerated carriers by improving light in-coupling and extending the effective optical path length. According to the Beer–Lambert law, light intensity decreases exponentially as it penetrates the material [49, 50]. In thin planar films or sparsely dispersed powder systems, incomplete photon utilization can occur because part of the incident light is transmitted, reflected, or scattered away before being absorbed. Consequently, optical architectures that enhance light trapping and extend the effective optical path length can improve the generation of usable photocarriers. Therefore, relying solely on the optimization of intrinsic material properties is insufficient. It is imperative to integrate optical strategies that enhance photon trapping and extend the effective optical path length, thereby maximizing η_{abs} and ultimately realizing high-efficiency photocatalytic systems.

Efficient solar energy harvesting fundamentally requires a strategic alignment between the semiconductor's intrinsic absorption and the incident solar spectrum. The magnitude of a semiconductor's bandgap determines the maximum wavelength of light it can absorb. Although narrowing the bandgap enables the harvesting of a broader portion of the visible-light spectrum, thereby increasing the theoretical limit of photogenerated charge carriers [51, 52], incident photons immediately face optical losses at the material's interface [53]. Perovskites possess a high refractive index (n) ranging from 2.0 to 2.5 in the visible-light region [54, 55], causing a severe mismatch with surrounding media such as air ($n \approx 1.0$) or aqueous solutions ($n \approx 1.33$). According to the Fresnel equations, this mismatch results in a substantial portion of incident light being reflected and lost before penetrating the photocatalyst [56]. Thus, optimizing the fundamental bandgap must be coupled with surface engineering to effectively guide light into the material's interior.

Once the incident light successfully penetrates the surface, a fundamental tradeoff between light absorption and charge transport within the bulk material must be resolved. Building upon the Beer–Lambert principles discussed earlier, maximizing light absorption requires the physical thickness of the photocatalyst to be greater than its optical penetration depth. Simultaneously, to ensure that photogenerated charges migrate to the surface without recombination, this thickness must be less than the charge-carrier diffusion length. The critical issue is that for semiconductor materials, including perovskites, the optical penetration depth can exceed the charge-carrier diffusion length [57]. In such scenarios, increasing the thickness to capture more light results in the bulk recombination of deeply generated charges, whereas reducing the thickness to facilitate charge collection leads to severe optical transmission losses [50].

This inherent dilemma cannot be addressed solely through adjustments to chemical composition. Therefore, a comprehensive approach integrating intrinsic material optimization with advanced optical engineering is imperative. To this end, this review categorizes light-utilization strategies into four design principles. “Electronic Structure Engineering” establishes the intrinsic foundation by tailoring compositional features, crystallographic dimensionality, and defect states to regulate bandgaps, band-edge positions, carrier dynamics, and surface reaction energetics. Building upon this optimized material basis, “Interfacial Design for Photocarrier Separation and Band Alignment” discusses Type-II, Z-scheme, and S-scheme heterojunctions that

28359399, 0, Downloaded from https://onlinelibrary.wiley.com/doi/10.1002/ece2.70090 by Chung-Ang University, Wiley Online Library on [02/08/2026]. See the Terms and Conditions (https://onlinelibrary.wiley.com/terms-and-conditions) on Wiley Online Library for rules of use; OA articles are governed by the applicable Creative Commons License

promote charge separation while preserving the redox driving force required for CO_2 reduction. "Structural Optical and Spin-Selective Engineering" then addresses extrinsic architectures, including porous scaffolds, hollow structures, ordered photonic crystals, inverse opals, and chiral structures, which enhance light trapping, extend the effective optical path length, facilitate CO_2 transport, and suppress recombination through spin-selective pathways. Finally, "Plasmonic Enhancement and Metal-Semiconductor Synergy" provides additional routes to expand light utilization and accelerate charge transfer through near-field amplification, hot-electron injection, and plasmonic mediation in heterojunction systems. By systematically connecting these four strategies, this review presents an integrated design roadmap for realizing efficient, selective, and stable halide perovskite photocatalysts for CO_2 photoreduction.

3 | Electronic Structure Engineering

Achieving high-efficiency photocatalytic CO_2 reduction requires a semiconductor with an optimal electronic band structure: a bandgap narrow enough to harvest a broad spectrum of visible light, yet wide enough to provide the thermodynamic driving force for the redox reactions. Conventional metal oxide photocatalysts, such as TiO_2 and ZnO, are intrinsically limited by their wide bandgaps ($E_g > 3.0$ eV) [58, 59]. This restricts their photoactivity primarily to the ultraviolet (UV) region, which accounts for less than 5% of the total solar spectrum, thereby limiting their maximum theoretical efficiency [60, 61].

In this context, halide perovskites have emerged as promising candidates due to their exceptional electronic and optical tunability. Unlike binary oxides, the unique ABX_3 crystal structure of perovskites allows continuous and precise engineering of the electronic band structure over a wide visible-to-near-infrared (NIR) range while retaining favorable charge-transport properties [52, 62, 63]. Importantly, this tunability is not limited to simple bandgap narrowing. The band-edge positions, orbital hybridization, crystallographic dimensionality, defect states, and carrier-trapping pathways collectively determine whether photogenerated electrons can be efficiently utilized for CO_2 reduction.

Therefore, this section discusses electronic structure engineering as a broader design strategy rather than limiting the discussion to bandgap engineering alone. First, compositional tuning is introduced as a direct approach for regulating bandgaps and band-edge positions through A-site, B-site, and X-site substitution. Second, crystallographic dimensionality control is discussed as a means of modifying quantum confinement, dielectric confinement, and direct/indirect-bandgap characteristics. Third, defect passivation and defect-mediated charge control are examined by distinguishing detrimental deep-level defects from intentionally regulated shallow defects or vacancies that can promote charge separation, intermediate adsorption, and reaction kinetics.

3.1 | Compositional Engineering

Compositional engineering represents the most fundamental and direct approach to tuning the optoelectronic properties of halide perovskites. The versatility of the perovskite crystal structure accommodates a wide range of ionic radii, allowing the formation of solid solutions through the substitution of cations (A and B sites) or anions (X site). According to molecular orbital theory, the valence-band maximum (VBM) of halide perovskites is primarily derived from the antibonding hybridization of the metal s orbitals and halide p orbitals, whereas the conduction-band minimum (CBM) is dominated by the metal p orbitals [64, 65].

Therefore, systematically replacing the halide anions (e.g., Cl^-, Br^-, and I^-) [66–68] or the metal cations (e.g., Pb^{2+}, Sn^{2+}, Bi^{3+}, and Sb^{3+}) [69, 70] directly modulates the orbital overlap and the resulting bandgap energy (E_g). This formation of mixed-composition solid solutions typically follows Vegard's law, as reflected by the linear evolution of lattice parameters with composition, and can allow continuous tuning of the absorption edge [71]. For instance, increasing the iodide content in a mixed-halide system reduces the bandgap, thereby shifting absorption toward lower-energy photons, whereas incorporating specific B-site metals can transform the bandgap nature from indirect to direct [72]. This section therefore focuses on compositional strategies that directly regulate intrinsic band structures and band-edge energetics for CO_2 photoreduction.

Lee et al. utilized X-site mixing to modulate the bandgap and electronic structure, while further optimizing it through B-site mixing to achieve a precisely tuned electronic structure. First, they focused on the effects of X-site mixing within the lead-free halide perovskite lattice as a primary means of bandgap modulation [73]. They developed $Cs_3Sb_2Cl_xBr_{9-x}$ mixed-halide perovskites by incorporating bromide (Br^-) into the $Cs_3Sb_2Cl_9$ lattice, marking the first report of CO_2 reduction using antimony-based mixed-halide perovskites (Figure 2a). As the Br^- content increased, the lattice underwent expansion due to the larger ionic radius of Br^- compared to Cl^- (Figure 2b). This halide mixing reduced the degree of octahedral distortion, which, in turn, enhanced the electronic distribution and facilitated improved CO_2 adsorption and activation (Figure 2c). Although the pristine $Cs_3Sb_2Cl_9$ and $Cs_3Sb_2Br_9$ phases exhibit indirect and direct bandgaps, respectively, the specific electronic nature of the mixed-halide phases remained unexplored. Thus, the researchers analyzed the evolution of the bandgap characteristics as a function of the Cl/Br ratio. The VB is primarily composed of Br 4p and Cl 3p orbitals, whereas the CB is dominated by Sb 5p and Br 4p contributions (Figure 2d). Increasing the Cl content results in bandgap widening and a subsequent blueshift of the absorption edge. Notably, the introduction of Br induces a transition toward a direct bandgap, enabling more efficient light harvesting than the pure chloride phase and significantly enhancing photocatalytic activity. Consequently, the optimized $Cs_3Sb_2Cl_4Br_5$ composition achieved a CH_4 yield of 4.92 μmol g^{-1} after 6 h of visible-light irradiation, representing a fourfold increase in photoreduction activity compared to $Cs_3Sb_2Cl_9$ (Figure 2e).

In a subsequent study, the research team evaluated the photocatalytic properties of a bimetallic perovskite synthesized by incorporating Bi alongside Sb at the B site (Figure 2f) [74]. The introduction of Bi into the previously optimized $Cs_3Sb_2Cl_4Br_5$ framework induced an upward shift of the Br p orbitals, further extending the light absorption range within the visible

28359399, 0, Downloaded from https://onlinelibrary.wiley.com/doi/10.1002/ece2.70090 by Chung-Ang University, Wiley Online Library on [02/08/2026]. See the Terms and Conditions (https://onlinelibrary.wiley.com/terms-and-conditions) on Wiley Online Library for rules of use; OA articles are governed by the applicable Creative Commons License

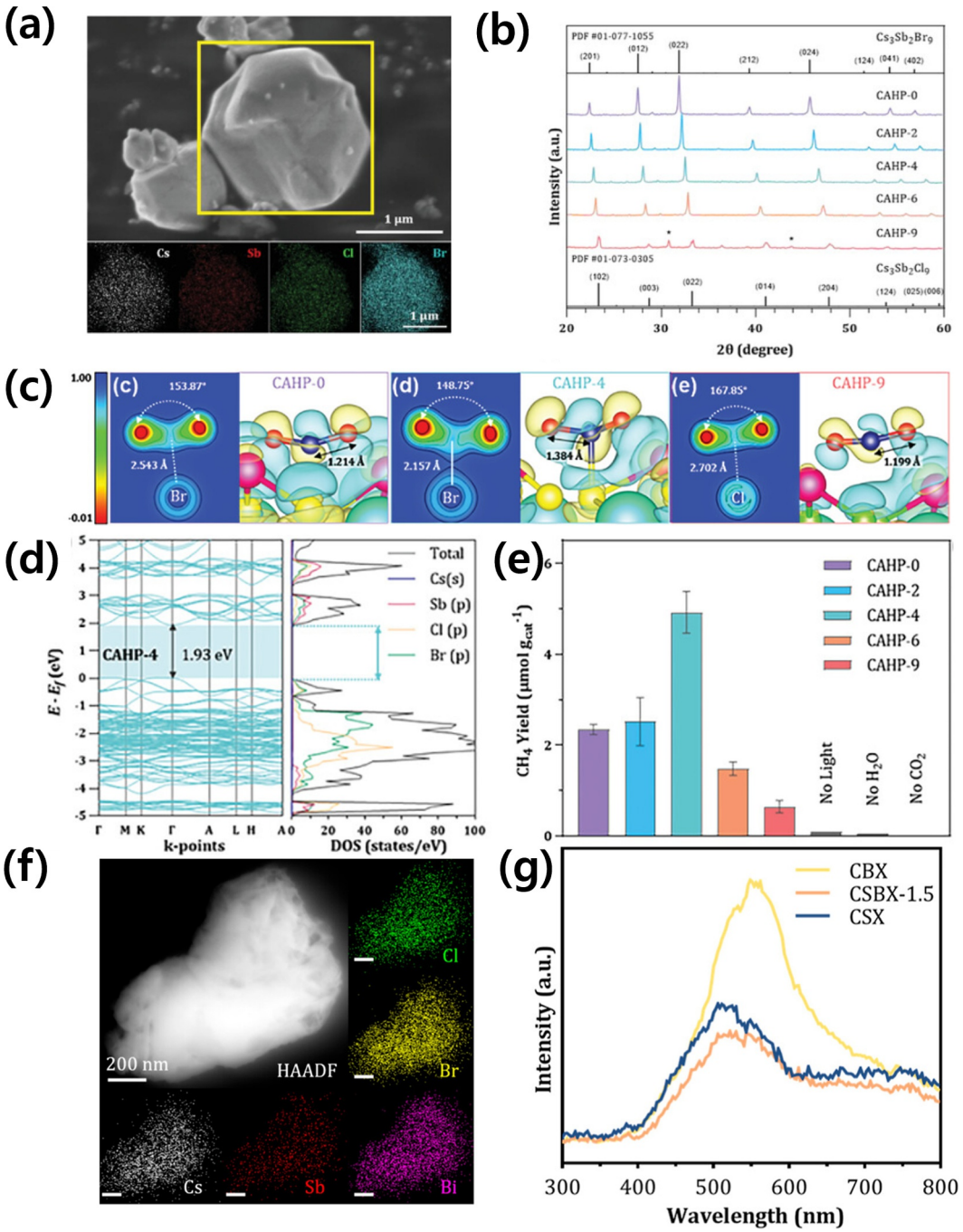


FIGURE 2 | Representative examples of compositional engineering in halide perovskite photocatalysts. (a) SEM image and elemental mapping of mixed-halide antimony-based perovskite particles. (b) XRD patterns of mixed-halide compositions, indicating composition-dependent structural evolution. (c) Electron localization and structural distortion in the Br-rich composition. (d) Calculated band structure and density of states of the representative mixed-halide composition. (e) Photocatalytic CH_4 yield of the mixed-halide perovskites under different conditions. Reproduced with permission [73]. Copyright 2023, John Wiley and Sons. (f) HAADF-STEM image and elemental mapping of the Bi-incorporated mixed-halide perovskite, confirming the homogeneous distribution of Cs, Sb, Bi, Cl, and Br. (g) Photoluminescence spectra of the Bi-alloyed compositions. Reproduced with permission [74]. Copyright 2024, American Chemical Society.

spectrum. From an electronic structure perspective, although the CB of the original material was governed by the p orbitals of Sb, Br, and Cl, the incorporation of Bi mitigated the dominant contribution of Sb atoms at the lower edge of the CB. This orbital reconstruction enhanced charge delocalization and significantly facilitated electronic transport within the lattice. Furthermore, analysis of the photoexcited charge-carrier behavior revealed the most pronounced PL quenching and the longest carrier lifetimes in the Bi-incorporated system (Figure 2g). Notably, the high photoinduced absorption signals and slow decay characteristics indicate that a large population of photoexcited carriers remains stable without undergoing immediate recombination. This stability is highly advantageous for photocatalytic CO_2 reduction, which typically requires

28359399, 0, Downloaded from https://onlinelibrary.wiley.com/doi/10.1002/ece2.70090 by Chung-Ang University, Wiley Online Library on [02/08/2026]. See the Terms and Conditions (https://onlinelibrary.wiley.com/terms-and-conditions) on Wiley Online Library for rules of use; OA articles are governed by the applicable Creative Commons License

multielectron-transfer processes. As a result, the optimized $Cs_3Sb_{0.5}Bi_{1.5}Cl_4Br_5$ photocatalyst yielded 6.28 μmol g^{-1} of CH_4 under 6 h of visible-light irradiation, surpassing the performance of its single-metal B-site counterparts.

3.2 | Crystallographic and Dimensionality Engineering

Although compositional engineering directly modulates the intrinsic band structure through atomic substitution, crystallographic dimensionality control provides another powerful strategy for regulating the optical and electronic properties of halide perovskites. In this subsection, dimensionality refers specifically to the connectivity of metal-halide octahedra within the crystal lattice, such as three-dimensional (3D), two-dimensional (2D), or layered perovskite frameworks, rather than the external morphology of nanocrystals or quantum dots. This distinction is important because morphological nanostructures, such as nanodots confined in porous matrices, primarily affect surface area, mass transfer, and interfacial charge separation, whereas crystallographic dimensionality directly modifies orbital coupling, quantum confinement, dielectric confinement, and band dispersion. Conventional 3D perovskites often exhibit strong visible-light absorption and favorable charge transport, but their photocatalytic applications can be limited by structural instability and rapid charge recombination under reaction conditions [75–77]. To overcome these limitations, researchers have explored low-dimensional and layered perovskite structures, particularly two-dimensional Ruddlesden–Popper (RP) phases, in which inorganic metal-halide octahedral sheets are separated by spacer cations [78–80]. This layered arrangement naturally forms a multiple-quantum-well architecture and induces strong quantum and dielectric confinement effects perpendicular to the inorganic layers [81, 82]. By precisely controlling the thickness of the 2D layers, denoted by the *n* value, researchers can strategically modulate the degree of quantum confinement [83]. Increasing the n value effectively narrows the bandgap and shifts the absorption edge toward longer wavelengths, allowing enhanced visible-light harvesting. Crucially, this tunability enables the optimization of light absorption properties while preserving the superior environmental and optical stability characteristic of 2D architectures.

As a representative example of crystallographic dimensionality control, Lin and colleagues designed all-inorganic RP perovskites (IRPPs) by introducing inorganic cesium ions as spacers instead of conventional organic molecules [84]. Although the synthesis of high-order IRPPs is challenging due to phase instability, the team achieved structural stabilization by employing octadecanedioic acid, a bidentate ligand with strong binding affinity, as a surface capping agent. This strategy enabled the successful synthesis of phase-pure $n = 3$ ($Cs_4Pb_3Br_{10}$) and $n = 4$ ($Cs_5Pb_4Br_{13}$) nanosheets (Figure 3a). Notably, as the number of inorganic layers increased from 3 to 4, the quantum confinement effect was effectively relaxed, leading to a consistent redshift of the absorption edge. This shift played a pivotal role in directly enhancing visible-light-harvesting efficiency. When evaluated as composites with reduced graphene oxide (RGO), the $n = 4$ structure exhibited superior photocatalytic activity of 81.39 μmol g^{-1}, surpassing the 54.82 μmol g^{-1} recorded for the $n = 3$ counterpart (Figure 3b). In addition to high activity, the catalysts demonstrated exceptional durability, maintaining 95% ($n = 3$) and 94% ($n = 4$) of their initial activity even after five consecutive cycles totaling 30 h (Figure 3c). These findings demonstrate that controlling the number of connected inorganic layers in RP perovskites can tune quantum confinement and visible-light absorption while improving structural durability during CO_2 photoreduction.

Another pivotal strategy in dimensionality control involves guiding a conventional 3D lattice into a layered crystal architecture to manipulate the intrinsic electronic structure and

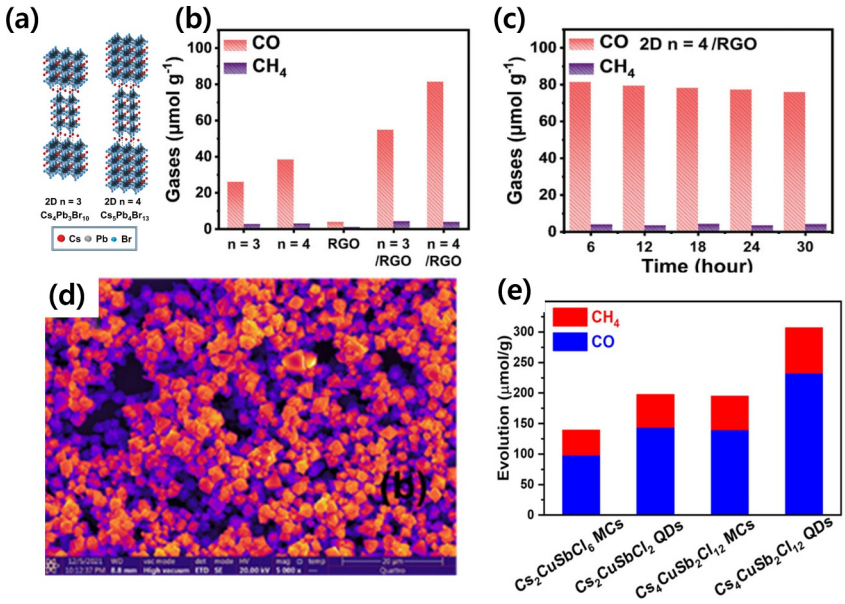


FIGURE 3 | (a) Crystal structures of low-dimensional all-inorganic Ruddlesden–Popper perovskites with different *n* values. (b) Photocatalytic CO and CH_4 production of layered perovskites and their RGO composites. (c) Time-dependent photocatalytic performance of the 2D $n = 4$/RGO system. Reproduced with permission [84]. Copyright 2022, John Wiley and Sons. (d) FESEM image of $Cs_4CuSb_2Cl_{12}$ QDs. (e) CO2 reduction performance of $Cs_4CuSb_2Cl_{12}$. Reproduced with permission [85]. Copyright 2022, John Wiley and Sons.

28359399, 0, Downloaded from https://onlinelibrary.wiley.com/doi/10.1002/ece2.70090 by Chung-Ang University, Wiley Online Library on [02/08/2026]. See the Terms and Conditions (https://onlinelibrary.wiley.com/terms-and-conditions) on Wiley Online Library for rules of use; OA articles are governed by the applicable Creative Commons License

charge-transport properties of the material. This approach is highly significant because structural transformation can fundamentally alter optical characteristics, such as converting an indirect bandgap into a direct bandgap, even when the constituent elements remain identical. Applying this concept to a lead-free Cu-Sb-based double perovskite, Wu and colleagues synthesized and systematically compared a 3D-networked $Cs_2CuSbCl_6$ with a layered $Cs_4CuSb_2Cl_{12}$ [85]. Structurally, $Cs_2CuSbCl_6$ adopts a 3D-networked framework, whereas $Cs_4CuSb_2Cl_{12}$ forms a layered crystal structure with distinct octahedral connectivity (Figure 3d). Interestingly, despite possessing similar bandgap magnitudes ranging from 1.65 to 1.67 eV, the two materials exhibit fundamentally different optical natures. The 3D $Cs_2CuSbCl_6$ displays an indirect bandgap, whereas the layered $Cs_4CuSb_2Cl_{12}$ features a direct bandgap. When evaluating their photocatalytic activities under 300 W Xe-lamp irradiation, the layered $Cs_4CuSb_2Cl_{12}$ demonstrated superior performance, yielding 223 μmol g^{-1} of CO and 74 μmol g^{-1} of CH_4 over 3 h (Figure 3e), significantly outperforming its 3D counterpart. This enhanced efficiency is attributed to two primary factors. First, the direct-bandgap nature enables highly efficient photoelectron generation without requiring phonon participation. Second, the platelet-shaped morphology effectively shortens the diffusion path for photogenerated charges to reach the surface active sites, thereby minimizing recombination losses.

3.3 | Defect Passivation and Defect-Mediated Charge Control

Defects play a dual role in halide perovskite photocatalysts. On one hand, uncontrolled defects, such as halide vacancies, undercoordinated metal ions, and deep-level trap states, can accelerate carrier recombination and destabilize the perovskite lattice. In this case, defect passivation is essential for suppressing recombination losses and preserving the population of photogenerated carriers available for surface redox reactions. On the other hand, carefully regulated shallow defects, vacancies, dopants, or lattice strain can serve as charge-control sites that promote carrier separation, tune the local electronic structure, and facilitate the adsorption or activation of CO_2 reduction intermediates [86]. Therefore, defect-related strategies should not be described simply as either beneficial or detrimental. Their function depends strongly on their energetic depth, spatial distribution, concentration, and interaction with surface reactions. Deep trap states generally act as recombination centers and should be passivated, whereas shallow or catalytically active defect states can participate in charge extraction or intermediate stabilization when their density is precisely controlled.

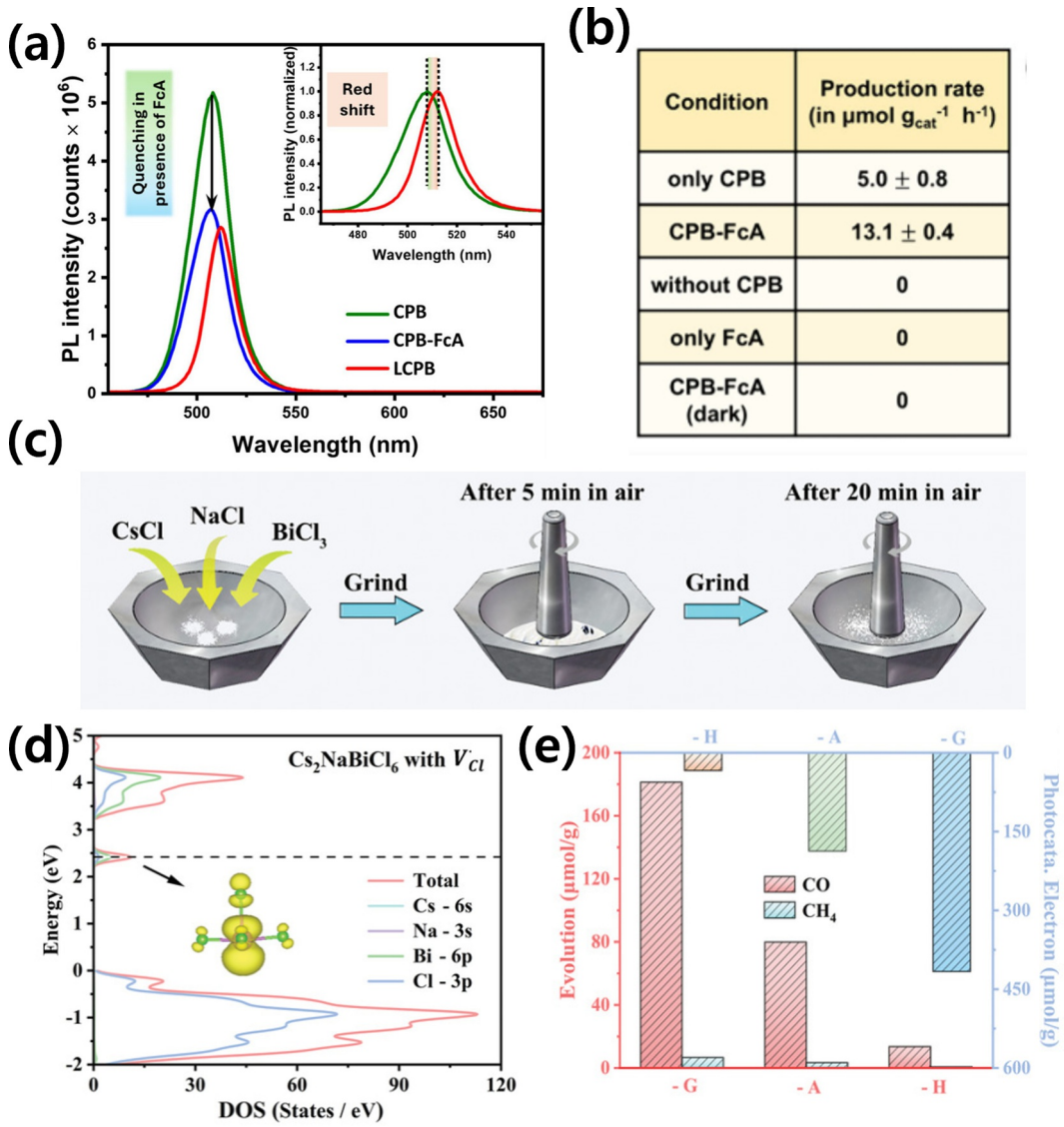
A representative example of dopant-mediated charge control is Mn-doped $CsPb(Br/Cl)_3$ perovskite. Although this system was previously discussed in the context of compositional engineering, its primary contribution is more closely associated with carrier dynamics than with simple bandgap tuning. Liu et al. synthesized Mn-doped $CsPb(Br/Cl)_3$ by introducing $MnCl_2$ during the synthesis of $CsPbBr_3$ [87]. With increasing doping concentration, the photoluminescence peak positions remained relatively stable, whereas the PL intensity decreased markedly. This PL quenching indicates suppressed radiative recombination and improved charge separation. When evaluated for CO_2 photoreduction in ethyl acetate under visible-light irradiation, the optimized Mn-doped $CsPb(Br/Cl)_3$ exhibited CO and CH_4 production rates of 1917 μmol g^{-1} and 82 μmol g^{-1}, respectively, corresponding to a 14.2-fold enhancement compared with pristine $CsPbBr_3$. This result demonstrates that dopant-mediated defect regulation can improve photocatalytic performance by modifying recombination pathways and charge separation behavior.

Moving beyond the conventional goal of defect elimination through passivation, controlled surface functionalization can also be used to regulate defect-mediated charge transfer. For instance, Singh et al. reported a study in which photocatalytic efficiency was substantially improved by anchoring ferrocenecarboxylic acid (FcA) to the surface of $CsPbBr_3$ nanocrystals and simultaneously inducing Br vacancies [88]. The introduction of FcA facilitates the migration of photogenerated holes to the FcA molecules, which maximizes charge separation and effectively suppresses exciton loss via radiative recombination (Figure 4a). Additionally, treatment with Pb-oleate was utilized to increase the ratio of undercoordinated lead atoms on the surface, which intentionally enriched the density of halide defects. These nanocrystals, featuring specifically targeted and enhanced defects, exhibited more than a twofold increase in catalytic activity compared to the untreated pristine material (Figure 4b). This case indicates that surface defects can be beneficial when their concentration and chemical environment are carefully controlled.

In a similar way, Pi and colleagues reported a study on regulating the photocatalytic reaction kinetics of lead-free double perovskites by controlling Cl vacancies [89]. The research team introduced $Cs_2NaBiCl_6$ as a photocatalyst and utilized different synthesis methods to elucidate performance variations depending on the defect concentration. Specifically, they compared three types of samples: $Cs_2NaBiCl_6$-H prepared via a hydrothermal method, $Cs_2NaBiCl_6$-A with minor defects induced through annealing, and $Cs_2NaBiCl_6$-G with a maximized defect density achieved through grinding (Figure 4c). Density functional theory (DFT) calculations revealed that the abundantly formed Cl defects created new localized defect levels within the bandgap, originating from the hybridization of Bi 6p and Cl 3p orbitals (Figure 4d). This modification narrowed the bandgap to significantly increase visible-light absorption and induced a Fermi-level upshift, which strengthened the n-type character and established a band structure highly favorable for electron transfer. Beyond these optoelectronic changes, the chlorine vacancies exerted a profound influence on the reaction thermodynamics. Notably, the Gibbs free energy barrier for the formation of the $COOH^*$ intermediate, which is the key rate-determining step in CO_2 reduction, was reduced from 1.808 to 0.616 eV. Owing to the synergistic effect between defect engineering and the material's intrinsic 3D hierarchical porous structure, the defect-rich $Cs_2NaBiCl_6$-G sample achieved an impressive CO production rate of 30.22 μmol g^{-1} h^{-1} without the use of sacrificial agents (Figure 4e). This result represents a 12-fold enhancement in photocatalytic activity compared to the defect-free counterpart.

Another innovative method for defect-mediated charge control is lattice-strain engineering. Fang and colleagues induced

28359399, 0, Downloaded from https://onlinelibrary.wiley.com/doi/10.1002/ece2.70090 by Chung-Ang University, Wiley Online Library on [02/08/2026]. See the Terms and Conditions (https://onlinelibrary.wiley.com/terms-and-conditions) on Wiley Online Library for rules of use; OA articles are governed by the applicable Creative Commons License



Condition	Production rate (in μmol g_{cat}^{-1} h^{-1})
only CPB	5.0 ± 0.8
CPB-FcA	13.1 ± 0.4
without CPB	0
only FcA	0
CPB-FcA (dark)	0

FIGURE 4 | (a) Photoluminescence spectra of pristine and FcA-modified $CsPbBr_3$, showing PL quenching and a spectral shift after surface functionalization. (b) Comparison of photocatalytic production rates under different control conditions. Reproduced with permission [88]. Copyright 2024, American Chemical Society. (c) Schematic illustration of the mechanochemical synthesis route for vacancy-engineered $Cs_2NaBiCl_6$-G. (d) Calculated density of states of Cl-vacancy-containing $Cs_2NaBiCl_6$. (e) Comparison of CO and CH_4 evolution and photoelectron generation for samples prepared under different synthesis methods. Reproduced with permission [89]. Copyright 2022, John Wiley and Sons.

structural strain within $CsPbBr_3$ QD particles by partially substituting Pb atoms with Cu [90]. This size mismatch generates compressive strain within the $(PbBr_6)^{4-}$ octahedral framework, leading to a modified electronic band structure. Crucially, this structural strain introduces shallow trap states rather than deep-level recombination centers. Femtosecond transient absorption spectroscopy revealed that these Cu-induced defect states effectively trap photogenerated electrons, thereby prolonging the hot-carrier thermalization and defect-mediated trapping processes (Figure 5a,b). Consequently, these shallow traps act as stepping stones that guide photogenerated charges toward interfacial redox processes rather than bulk recombination, significantly enhancing charge separation efficiency (Figure 5c). Furthermore, this lattice strain fundamentally alters the surface thermodynamic properties. DFT calculations indicated that the compressive strain induces an upward shift of the d-band center, which strengthens the adsorbate–substrate interactions. In the context of CO_2 photoreduction, this strained surface effectively lowers the formation energy of key intermediates such as *COOH, thermodynamically favoring the catalytic conversion pathway (Figure 5d). As a direct consequence of this engineered structure, the $CsPb_{0.9}Cu_{0.1}Br_3$ catalyst demonstrated remarkably enhanced photocatalytic CO_2 reduction performance. It achieved high evolution rates of CO and CH4 (69.75 and 25.84 μmol g^{-1} within 3 h, respectively) with a notable CO selectivity of 74%. This study comprehensively demonstrates that surface defects and lattice strain in perovskites are not necessarily detrimental features that should be suppressed. Instead, when integrated with atomic-level structural engineering, they can serve as excellent active sites that simultaneously optimize carrier dynamics and drive substrate-specific photocatalytic reactions.

28359399, 0, Downloaded from https://onlinelibrary.wiley.com/doi/10.1002/ece2.70090 by Chung-Ang University, Wiley Online Library on [02/08/2026]. See the Terms and Conditions (https://onlinelibrary.wiley.com/terms-and-conditions) on Wiley Online Library for rules of use; OA articles are governed by the applicable Creative Commons License

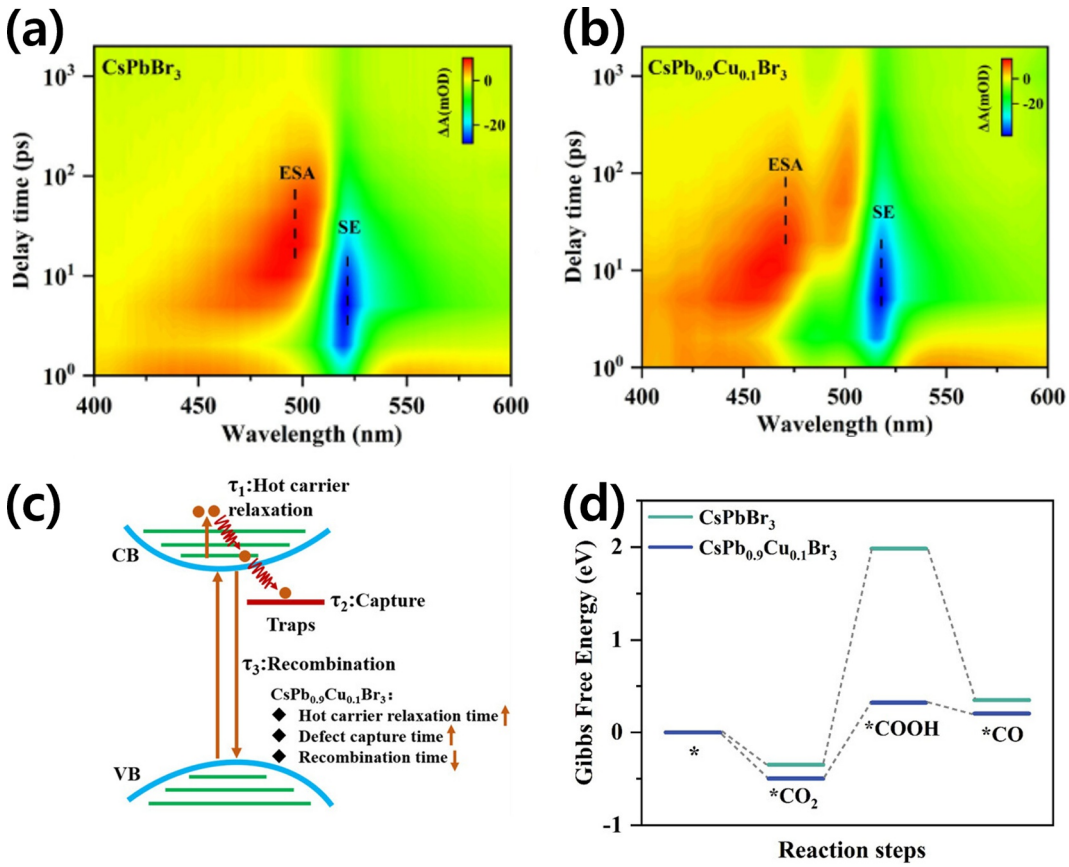


FIGURE 5 | Defect engineering and band alignment through lattice strain and heterojunction formation. Transient absorption map of pristine $CsPbBr_3$ (a) and $CsPb_{0.9}Cu_{0.1}Br_3$ (b). (c) Schematic illustration of carrier relaxation, trap capture, and recombination processes in $CsPb_{0.9}Cu_{0.1}Br_3$. (d) Calculated Gibbs free energy diagram for CO_2 reduction on pristine $CsPbBr_3$ and $CsPb_{0.9}Cu_{0.1}Br_3$. Reproduced with permission [90]. Copyright 2025, American Chemical Society.

Overall, defect-related strategies in halide perovskite photocatalysts should be understood through the balance between passivation and controlled defect utilization. Deep-level defects and uncontrolled surface vacancies generally accelerate nonradiative recombination and should be passivated, whereas intentionally regulated shallow defects, dopants, vacancies, and lattice strain can promote charge separation, tune local electronic states, and lower reaction barriers for CO_2 reduction. Therefore, the key design principle is not simply to eliminate all defects but to suppress detrimental recombination centers while preserving or generating beneficial defect states that participate in charge transfer and catalytic intermediate stabilization.

4 | Interfacial Design for Photocarrier Separation and Band Alignment

Although electronic structure engineering can optimize the intrinsic bandgap and redox potential of halide perovskites, the overall photocatalytic efficiency is often governed by how efficiently photogenerated carriers are separated and transferred to surface reaction sites. This point is particularly important for CO_2 photoreduction because the reaction proceeds through sluggish multielectron/proton-coupled pathways and therefore requires long-lived charge carriers as well as appropriate interfacial energetics [35]. In practical perovskite photocatalysts, rapid electron–hole recombination, insufficient interfacial charge extraction, and weak adsorption and activation of CO_2 intermediates remain major kinetic bottlenecks, even when the material possesses strong visible-light absorption.

Heterojunction construction provides a direct route to address these limitations by coupling perovskites with semiconductors, carbon-based conductors, or catalytic supports possessing different Fermi levels and band-edge positions. Once two components come into contact, interfacial charge redistribution occurs until Fermi-level equilibrium is reached, producing band bending and an internal electric field that can drive directional carrier migration [91]. Depending on the relative band alignment and charge-transfer pathway, perovskite-based heterojunctions can be classified into Type-II, Z-scheme, and S-scheme systems. These architectures differ not only in how they separate electrons and holes but also in whether they preserve or sacrifice the redox power of the photogenerated carriers. Therefore, this section discusses interfacial design strategies by comparing their charge-transfer mechanisms, thermodynamic advantages, and limitations for photocatalytic CO_2 reduction.

4.1 | Type-II Heterojunctions

Type-II heterojunctions are among the most straightforward interfacial architectures for suppressing charge recombination. In a typical staggered band alignment, the conduction-band minimum and valence-band maximum of one semiconductor are positioned higher than those of the other component. Upon

28359399, 0, Downloaded from https://onlinelibrary.wiley.com/doi/10.1002/ece2.70090 by Chung-Ang University, Wiley Online Library on [02/08/2026]. See the Terms and Conditions (https://onlinelibrary.wiley.com/terms-and-conditions) on Wiley Online Library for rules of use; OA articles are governed by the applicable Creative Commons License

photoexcitation, electrons migrate from the higher conduction band to the lower conduction band, whereas holes transfer in the opposite direction from the lower valence band to the higher valence band. This spatial separation of electrons and holes reduces their recombination probability and increases the lifetime of carriers available for surface redox reactions.

A representative example is the all-zero-dimensional $CsPbBr_3$/CdSe heterojunction reported by Yin et al. [92]. In this system, CdSe quantum dots were grown in situ on $CsPbBr_3$ quantum dots to form an intimate 0D/0D heterointerface. The resulting Type-II band alignment facilitated directional electron transfer across the interface, whereas strong Pb–Se and Br–Cd interfacial bonding promoted electronic coupling between the two components. Importantly, the CdSe component also provided abundant edge and corner sites that promoted CO_2 activation by forming Cd-C_2O_4 adducts. As a result, the $CsPbBr_3$/CdSe heterojunction achieved a CO yield of 115.26 μmol g^{-1}, which was 4.6 times higher than that of pristine $CsPbBr_3$. This example demonstrates that Type-II heterojunctions can improve photocatalytic CO_2 reduction not only by suppressing recombination but also by coupling charge separation with reactant activation.

A similar Type-II charge separation strategy was demonstrated in a conducting polymer/perovskite hybrid system. Li et al. encapsulated $CsPbBr_3$ QDs with P3HT to construct a P3HT/$CsPbBr_3$ composite, in which P3HT served as both a protective layer and a hole-transporting component [93]. The band alignment between P3HT and $CsPbBr_3$ forms a Type-II heterojunction: Photoexcited electrons in P3HT transfer to the conduction band of $CsPbBr_3$, whereas holes generated in $CsPbBr_3$ migrate to the HOMO level of P3HT. This spatial separation of charge carriers suppresses recombination, as evidenced by an enhanced photocurrent response, reduced charge-transfer resistance, PL quenching, and accelerated TRPL decay. Consequently, the P3HT/$CsPbBr_3$ composite achieved CO and CH_4 production rates of 145.45 and 23.05 μmol g^{-1} h^{-1}, respectively, with an electron consumption rate of 475.3 μmol g^{-1} h^{-1}, about ten times higher than that of pristine $CsPbBr_3$ QDs. In addition, the P3HT coating improved catalytic stability, maintaining the activity, crystal structure, and morphology after three consecutive cycles. This result highlights that polymer/perovskite Type-II interfaces can simultaneously promote charge separation and stabilize moisture-sensitive perovskite photocatalysts.

4.2 | Z-Scheme Heterojunctions

Unlike Type-II heterojunctions, Z-scheme heterojunctions are designed to achieve charge separation while preserving strong redox potentials. In this architecture, photogenerated electrons in the conduction band of the oxidation photocatalyst recombine with holes in the valence band of the reduction photocatalyst through a direct solid–solid interface or an electron mediator. As a result, the high-energy electrons with strong reduction ability and the holes with strong oxidation ability remain spatially separated on different components. This charge-transfer pathway is particularly advantageous for CO_2 photoreduction because the formation of products such as CO, CH_4, or HCOOH requires sufficiently negative electrons and multiple electron-transfer steps.

A clear example highlighting the advantage of Z-scheme charge transfer is the lead-free $Cs_2AgBiBr_6$@g-C_3N_4 system reported by Wang et al. [94]. By controlling the surface coverage of g-C_3N_4 on $Cs_2AgBiBr_6$ (CABB), the authors obtained two distinct interfacial pathways: CABB@g-C_3N_4-10% behaved as a Type-II heterojunction, whereas CABB@g-C_3N_4-82% operated as a Z-scheme system. In the Type-II structure, electrons migrated from g-C_3N_4 to CABB, favoring the two-electron CO_2-to-CO pathway. In contrast, the Z-scheme structure promoted recombination between electrons in CABB and holes in g-C_3N_4, thereby preserving strongly reducing electrons on the CB of g-C_3N_4 and oxidizing holes on the VB of CABB. As a result, CABB@g-C_3N_4-82% exhibited superior CH_4 production with CH_4 selectivity exceeding 70%, whereas the overall CO_2 reduction activity was 16-fold and 10-fold higher than those of pure CABB and g-C_3N_4, respectively. Surface photovoltage, in situ irradiated XPS, monochromatic-light activity tests, and transient photocurrent analyses supported the proposed Z-scheme pathway, demonstrating that the interfacial architecture can regulate not only charge separation but also product selectivity in perovskite-based CO_2 photoreduction.

4.3 | S-Scheme Heterojunctions

S-scheme heterojunctions have recently emerged as an advanced interfacial design strategy that combines efficient charge separation with strong redox capability. Similar to Z-scheme systems, S-scheme heterojunctions preserve high-energy electrons and holes, but their charge-transfer behavior is governed more explicitly by Fermi-level equilibration, band bending, and the resulting internal electric field at the interface. When two semiconductors with different work functions are brought into contact, electrons transfer from the component with a higher Fermi level to that with a lower Fermi level until equilibrium is established. This process induces built-in electric fields and interfacial band bending, which drive the recombination of low-redox-potential electrons and holes while retaining the strongly reducing electrons and strongly oxidizing holes [91].

A representative example is the TiO_2/$CsPbBr_3$ S-scheme heterojunction reported by Wang et al. [95]. In this study, $CsPbBr_3$ quantum dots were coupled with TiO_2 exposing different crystal facets, namely, T-101 and T-001, to investigate how facet-dependent Fermi-level modulation affects CO_2 photoreduction. Compared with T-001, T-101 exhibited a larger Fermi-level difference with $CsPbBr_3$, which generated a stronger internal electric field and more pronounced band bending at the TiO_2/$CsPbBr_3$ interface. This interfacial field promoted the S-scheme charge-transfer pathway, in which low-energy carriers recombined selectively, whereas high-energy electrons in the CB of $CsPbBr_3$ and strongly oxidizing holes in the VB of TiO_2 were retained. Consequently, the T-101/$CsPbBr_3$ composite achieved a CO production rate of 12.5 μmol h^{-1} with a CO selectivity of 90.2%, corresponding to a 15.6-fold enhancement over pristine T-101 and a 5.6-fold enhancement over the T-001/$CsPbBr_3$ counterpart. This result demonstrates that facet engineering can tune Fermi-level disparity and interfacial band bending, thereby optimizing S-scheme charge separation for CO_2 photoreduction.

28359399, 0, Downloaded from https://onlinelibrary.wiley.com/doi/10.1002/ece2.70090 by Chung-Ang University, Wiley Online Library on [02/08/2026]. See the Terms and Conditions (https://onlinelibrary.wiley.com/terms-and-conditions) on Wiley Online Library for rules of use; OA articles are governed by the applicable Creative Commons License

5 | Structural Optical and Spin-Selective Engineering

Although the previous section explored methodologies to optimize the intrinsic energy-band structure and charge separation dynamics of perovskites at the atomic and nanoscale, this section focuses on macroscopic and mesoscopic structural engineering strategies aimed at maximizing fundamental light–matter interactions.

The primary step in any photocatalytic process is the efficient harvesting of incident solar photons. Although halide perovskites possess an exceptionally high intrinsic absorption coefficient, simple bulk or planar catalytic morphologies inevitably suffer from severe optical losses due to surface reflection and transmission [96, 97]. To circumvent this, recent research has increasingly shifted toward designing sophisticated 3D optical architectures that physically trap incident light, promoting repeated scattering and prolonged residence within the catalytic matrix [98, 99].

In this section, we systematically discuss three advanced structural designs tailored for superior light management. First, we explore 'Porous scaffolds and hollow architectures,' which induce multiple light scattering events while simultaneously expanding the active surface area. Second, we examine 'Photonic crystals and ordered structures,' which enhance the absorption of specific wavelengths via the slow-photon effect. Finally, we delve into the emerging frontier of 'Chiral structures and spin selectivity,' which exploits optical asymmetry to generate spin-polarized electrons, thereby potentially suppressing charge recombination through spin-selective transport. These sophisticated architectural engineering strategies not only push the physical limits of light-harvesting capacity but also offer synergistic advantages in carrier dynamics, serving as a powerful platform for boosting photocatalytic CO_2 reduction.

5.1 | Porous Scaffolds and Hollow Architectures

The primary determinant of photocatalytic efficiency lies in how effectively incident solar light is absorbed without optical losses. Because halide perovskites typically possess a high intrinsic refractive index ($n_p \approx 2.0$–2.5), planar or solid bulk morphologies inevitably suffer from significant optical losses due to surface reflection. The surface reflectance (R) for normally incident light at the interface of two media is governed by the Fresnel equation,

$$R = \left(\frac{n_p - n_m}{n_p + n_m}\right)^2,$$

where n_p and n_m represent the refractive indices of the perovskite and the surrounding medium (e.g., air or aqueous media), respectively. A larger mismatch between n_p and n_m leads to a sharp increase in reflectance R, causing detrimental optical loss. The most intuitive strategy for drastically mitigating this reflection loss and confining the incident light is to engineer physical pores or cavities within the particles. Once light enters porous scaffolds or hollow architectures, it becomes trapped within the enclosed geometry, undergoing successive multiple reflections and scattering events instead of escaping. This light-trapping effect can be mathematically elucidated using a modified Beer–Lambert law.

$$A = 1 - e^{-\alpha d}$$

Although the optical absorption A of a conventional planar material relies on its physical thickness d, the multiple reflections within a 3D porous or hollow architecture significantly prolong the effective optical path length (L_{eff}) that light travels within the material, making it much greater than the actual physical dimension of the particle ($dL_{\text{eff}} \gg$).

$$A_{\text{porous}} = 1 - e^{-\alpha L_{\text{eff}}}$$

Consequently, even with an identical mass of photocatalyst, adopting a hollow or porous structural design allows the material to reabsorb the light that would otherwise be lost through surface reflection. This exponentially extends the duration of light–matter interactions, thereby maximizing the light-harvesting capacity. Furthermore, beyond these optical benefits, such architectures provide profound kinetic advantages by drastically expanding the active surface area, which facilitates the diffusion and robust adsorption of CO_2 molecules. This section explores a variety of 3D optical architectures, ranging from MOF-derived hollow structures (e.g., ZIF-67) to multishell geometries and highly porous aerogels. These architectures provide promising routes for improving the photocatalytic performance of perovskites.

A representative example of realizing this light-trapping effect involves the design of sophisticated hollow structures utilizing MOFs as sacrificial templates. Deng et al. successfully constructed a $CsPbBr_3/Co_3O_4$ (CPBCO) composite by synthesizing hollow polyhedral Co_3O_4 nanocages derived from ZIF-67 MOFs and subsequently anchoring $CsPbBr_3$ quantum dots onto their surfaces (Figure 6a) [100]. This unique hollow nanocage architecture serves as an excellent optical cavity. Incident visible light penetrates the hollow interior and undergoes continuous multiple reflections and scattering against the inner walls of the shell, thereby drastically extending the effective optical path length. Spectroscopic analyses revealed a marked enhancement in light absorption after the formation of the CPBCO composite, demonstrating that the hollow geometry played a decisive role in maximizing the visible-light-harvesting efficiency of the perovskite. Beyond optical advantages, this architecture provides an exceptionally large specific surface area with a thin, porous shell, facilitating the easy diffusion and robust adsorption of reactant CO_2 molecules onto both the exterior and interior surfaces. Furthermore, the p-n heterojunction formed between $CsPbBr_3$ and Co_3O_4 on the hollow shell, coupled with abundant oxygen vacancies, effectively separated the large number of photogenerated electrons generated by the spatially confined, highly concentrated light energy. As a result, the optimized CPBCO photocatalyst achieved an outstanding CO production rate of 55.82 μmol g^{-1} h^{-1} and a CH_4 production rate of 5.98 μmol g^{-1} h^{-1} (Figure 6b).

Beyond utilizing MOFs as sacrificial templates, strategies that induce the self-assembly of hollow spherical structures via antisolvent-assisted methods have also been successfully reported. Mu et al. synthesized lead-free halide perovskite hollow

28359399, 0, Downloaded from https://onlinelibrary.wiley.com/doi/10.1002/ece2.70090 by Chung-Ang University, Wiley Online Library on [02/08/2026]. See the Terms and Conditions (https://onlinelibrary.wiley.com/terms-and-conditions) on Wiley Online Library for rules of use; OA articles are governed by the applicable Creative Commons License

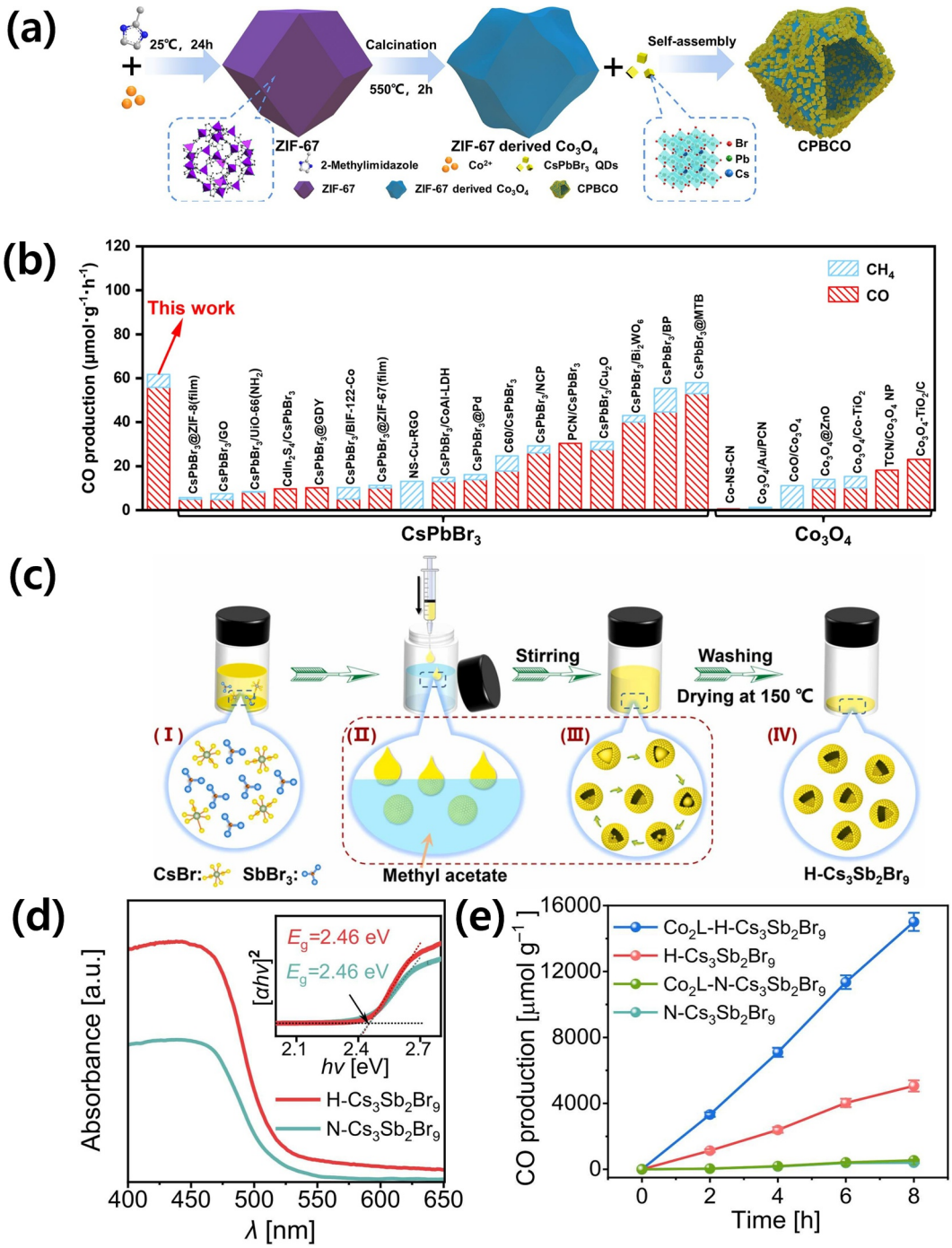


FIGURE 6 | Hollow architecture engineering for improved light harvesting and photocatalytic performance. (a) Schematic illustration of the synthesis of the hollow $CsPbBr_3/Co_3O_4$ photocatalyst derived from a ZIF-67 template. (b) Comparison of CO and CH_4 production rates of the hollow composite with reported reference systems. Reproduced with permission [100]. Copyright 2023, Elsevier. (c) Schematic illustration of the synthesis of hollow H-$Cs_3Sb_2Br_9$ particles. (d) UV–Vis absorption spectra and corresponding optical bandgap analysis of hollow and nonhollow $Cs_3Sb_2Br_9$. (e) Time-dependent CO production of hollow and nonhollow $Cs_3Sb_2Br_9$-based photocatalysts, showing the performance enhancement provided by the hollow architecture. Reproduced with permission [101]. Copyright 2023, Elsevier.

nanospheres (H-$Cs_3Sb_2Br_9$) and applied them to photocatalytic CO_2 reduction (Figure 6c) [101]. In this study, the hollow nanosphere architecture provided three critical advantages from both optical and kinetic perspectives. First, it maximized the light absorption capacity through multiple light scattering events within the interior cavity (Figure 6d). Second, the thin shell significantly shortened the migration distance of photogenerated carriers to the surface, thereby enhancing charge separation and charge-transfer efficiency. Third, it secured high surface reactivity by enlarging the specific surface area available for reactant adsorption. Upon illumination, the vast number of photoelectrons generated via multiple scattering rapidly migrated and accumulated at the Sb sites on the catalyst surface. When this architecture was coupled with a dinuclear

28359399, 0, Downloaded from https://onlinelibrary.wiley.com/doi/10.1002/ece2.70090 by Chung-Ang University, Wiley Online Library on [02/08/2026]. See the Terms and Conditions (https://onlinelibrary.wiley.com/terms-and-conditions) on Wiley Online Library for rules of use; OA articles are governed by the applicable Creative Commons License

cobalt molecular complex as a cocatalyst, the combination of optical benefits and charge extraction efficiency produced a strong synergy. Consequently, the optimized H-$Cs_3Sb_2Br_9$-based composite achieved an astonishing CO yield of 15 010.4 μmol g^{-1} over 8 h (Figure 6e). This represents a remarkable 28-fold enhancement compared to its solid nanocrystal counterpart, unequivocally demonstrating that confining light within a hollow nanosphere design is a highly potent key to overcoming the intrinsic performance limitations of lead-free perovskites.

Moving beyond single-shell hollow architectures, multishell configurations have historically offered groundbreaking geometric advantages in the field of photocatalysis. By strategically placing different cocatalysts on the inner and outer shells, these structures enable the complete physical and spatial separation of oxidation and reduction reaction zones. Simultaneously, they allow the robust physical encapsulation and protection of vulnerable internal photoactive materials from the external environment. Applying these profound structural advantages to moisture-sensitive halide perovskites, Feng et al. successfully designed a ternary heterojunction multishell hollow structure composed of $TiO_2/Cs_3Bi_2I_9$/g-C_3N_4 [102]. In this sophisticated architecture, the lead-free $Cs_3Bi_2I_9$ perovskite serves as the middle photoactive layer responsible for robust light harvesting (Figure 7a). Strategically, TiO_2 acts as the inner shell explicitly tailored for water oxidation, whereas g-C_3N_4 forms the outer shell dedicated to CO_2 reduction. This precise spatial separation efficiently extracts the photogenerated electrons and holes, which are produced by the trapped light within the multishell structure, in opposite directions, thereby fundamentally inhibiting charge recombination (Figure 7b). Crucially, this double-sided protection effectively shields the vulnerable perovskite lattice from moisture-induced degradation. Consequently, this multishell construct achieved an excellent CO production rate of 120.6 μmol g^{-1} h^{-1}, representing a 3.1-fold enhancement over the pristine perovskite (Figure 7c). Most remarkably, it demonstrated excellent long-term stability, operating without any noticeable activity decay for one hundred hours under harsh artificial photosynthesis conditions using water as the direct electron donor (Figure 7d).

In addition to hollow architectures, the utilization of 3D aerogels as a highly effective class and extreme form of porous scaffolds has also garnered significant attention. Li et al. constructed a massive 3D porous aerogel network by self-assembling highly conductive 2D MXene ($Ti_3C_2T_x$) nanosheets, onto which $CsPbBr_3$ nanocrystals were uniformly anchored [103]. The interconnected macroporous structure inherent to this aerogel maximizes light scattering to drastically enhance light absorption while simultaneously providing a highly favorable environment for the diffusion and adsorption of CO_2 gas. Combining the optical light-trapping effect with the exceptional charge extraction capability of the MXene framework, the composite achieved an outstanding electron consumption yield of 112.6 μmol g^{-1} h^{-1}. This clearly illustrates the profound impact of highly porous 3D scaffolds on both amplifying light harvesting and facilitating mass transfer.

Perovskite NCs intrinsically possess high surface energy, making them prone to severe aggregation and structural degradation during photocatalytic reactions. To address this, incorporating functional supports that can stably anchor and disperse the NCs is imperative. Choi et al. implemented a porous copper scaffold embedded with $CsPbBr_3$ to simultaneously achieve physical stabilization and optical amplification [104]. The intricate porous architecture of the copper scaffold induced multiple light scattering within the structure, resulting in superior light absorption compared to planar configurations (Figure 8a). Furthermore, in situ spectroscopic analysis revealed that the copper scaffold serves not only as a structural framework but also as an active cocatalyst that accepts electrons from the perovskite to facilitate C–C bond formation. Consequently, a remarkable shift in product selectivity from C1 (CH_4) to higher-value C2 products (C_2H_4 and C_2H_6) was observed (Figure 8b).

Studies utilizing organic and inorganic nanomaterials as supports to accelerate charge separation have also been reported. Zhang et al. designed a $C_{60}/CsPbBr_3$ composite by introducing C_{60} as both a support and an electron acceptor [105]. The large delocalized π-electron system of C_{60} enabled ultrafast extraction of photogenerated electrons from the perovskite, effectively suppressing charge recombination (Figure 8c). Simultaneously, C_{60} acted as a physical spacer to prevent particle aggregation, thereby ensuring long-term stability.

Additionally, Zhao et al. employed 2D layered double hydroxide (LDH) nanosheets as a robust support platform [106]. By firmly anchoring negatively charged $CsPbBr_3$ onto the positively charged NiAl-LDH surface via strong electrostatic interactions, they effectively prevented nanocrystal aggregation and maximized the active surface area. The LDH support not only facilitated charge transfer but also provided optical benefits by redshifting the absorption edge, enabling the composite to achieve a 3.7-fold enhancement in CO_2 reduction efficiency compared to pristine $CsPbBr_3$.

5.2 | Ordered Photonic Crystals and Inverse Opals

Although the previously discussed random porous structure relies on stochastic scattering to extend the optical path length, photonic crystals (PCs), constructed by periodically arranging dielectric media with contrasting refractive indices, offer a more sophisticated, wave-optical approach to manipulating light propagation. Representative architectures, such as opals or inverse opals, also known as 3D-ordered macroporous (3DOM) structures, possess a periodicity comparable to the wavelength of light. This periodicity establishes a photonic bandgap (PBG), a range of wavelengths in which light propagation is forbidden [107]. The most critical advantage of these structures lies in the 'slow photon effect' that occurs at the edges of the PBG [108]. When light with a wavelength near the bandgap edge enters the photonic crystal, its group velocity is drastically reduced due to multiple Bragg reflections and interference phenomena. These slowed photons exhibit a significantly prolonged residence time within the photocatalytic material, thereby enhancing the probability of photon–matter interaction and maximizing the apparent light-harvesting efficiency. Furthermore, the ordered and interconnected pore channels of 3DOM structures minimize diffusion resistance for electrolytes or gaseous reactants, creating an ideal environment for mass transfer. This section explores various instances of how such ordered architectures

28359399, 0, Downloaded from https://onlinelibrary.wiley.com/doi/10.1002/ece2.70090 by Chung-Ang University, Wiley Online Library on [02/08/2026]. See the Terms and Conditions (https://onlinelibrary.wiley.com/terms-and-conditions) on Wiley Online Library for rules of use; OA articles are governed by the applicable Creative Commons License

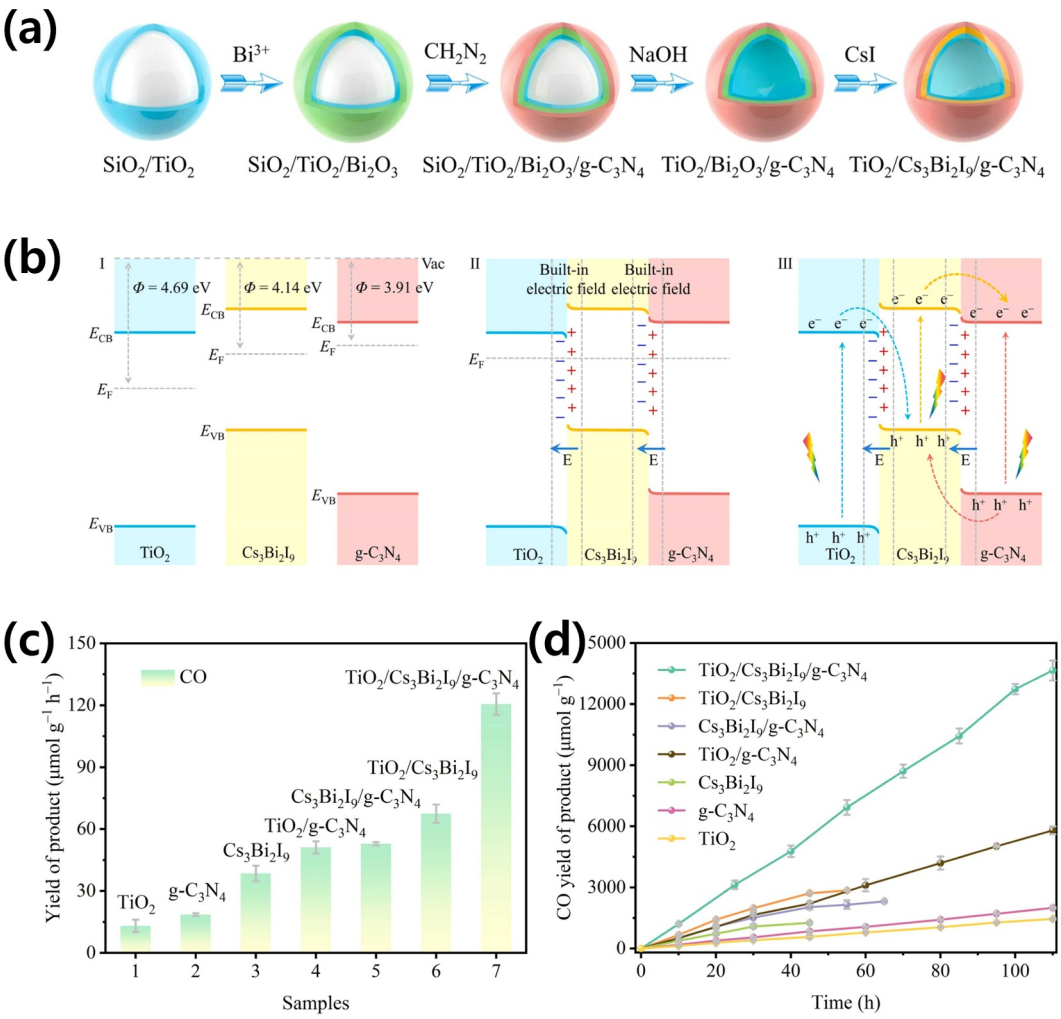


FIGURE 7 | Multishell hollow heterostructure for artificial photosynthesis. (a) Schematic illustration of the stepwise synthesis of the TiO_2/$Cs_3Bi_2I_9$/g-C_3N_4 multishell structure. (b) Energy-band alignment and charge-transfer pathway in TiO_2/$Cs_3Bi_2I_9$/g-C_3N_4. (c) Comparison of CO production over the individual components and TiO_2/$Cs_3Bi_2I_9$/g-C_3N_4. (d) Time-dependent CO production, demonstrating the superior activity of TiO_2/$Cs_3Bi_2I_9$/g-C_3N_4. Reproduced with permission [102]. Copyright 2024, Elsevier.

significantly enhance the light-harvesting capacity and CO_2 reduction performance of perovskites.

For CO_2 photoreduction, the key challenge is to translate this photonic light-management effect into improved charge utilization and catalytic stability. Pristine inverse-opal halide perovskites can, in principle, provide strong optical advantages through light scattering, slow-photon-assisted absorption, large surface area, and shortened carrier-diffusion pathways. However, their highly porous frameworks are often mechanically fragile and vulnerable to moisture-induced degradation. Therefore, effective inverse-opal design for perovskite CO_2 photoreduction must simultaneously address three requirements: enhanced photon trapping, efficient charge extraction, and structural robustness under reaction conditions.

A representative CO_2-focused example was reported by Han et al., who developed a robust and flexible free-standing $CsPbBr_3$ inverse-opal film by incorporating carbon dots (CDs) as mediating agents [109]. In this study, the IO architecture performs the fundamental functions of maximizing light harvesting through enhanced light scattering and multiple reflections (Figure 9a). The innovation lies in the role of the incorporated CDs, which reside at the perovskite grain boundaries, acting as "molecular bridges." These CDs firmly interconnect the grains, thereby enhancing the mechanical strength and imparting flexibility to the film while simultaneously serving as a protective barrier that significantly improves water resistance. Electrically, the CDs function as excellent electron acceptors, facilitating the rapid extraction and separation of electron–hole pairs generated within the IO structure. Driven by the synergy between optical architectural design and grain-boundary passivation, the optimized CDs/IO-$CsPbBr_3$ film achieved a CO production rate of 60.25 μmol g^{-1} h^{-1} (Figure 9b). This represents a 15.6-fold enhancement over the conventional $CsPbBr_3$ counterpart, demonstrating that photonic crystal structures can evolve beyond mere optical devices into durable, flexible photocatalytic platforms.

5.3 | Chiral Structures and Spin Selectivity

Although the structural engineering strategies discussed thus far have focused on controlling light scattering and mass transfer at macroscopic and mesoscopic scales, an emerging

28359399, 0, Downloaded from https://onlinelibrary.wiley.com/doi/10.1002/ece2.70090 by Chung-Ang University, Wiley Online Library on [02/08/2026]. See the Terms and Conditions (https://onlinelibrary.wiley.com/terms-and-conditions) on Wiley Online Library for rules of use; OA articles are governed by the applicable Creative Commons License

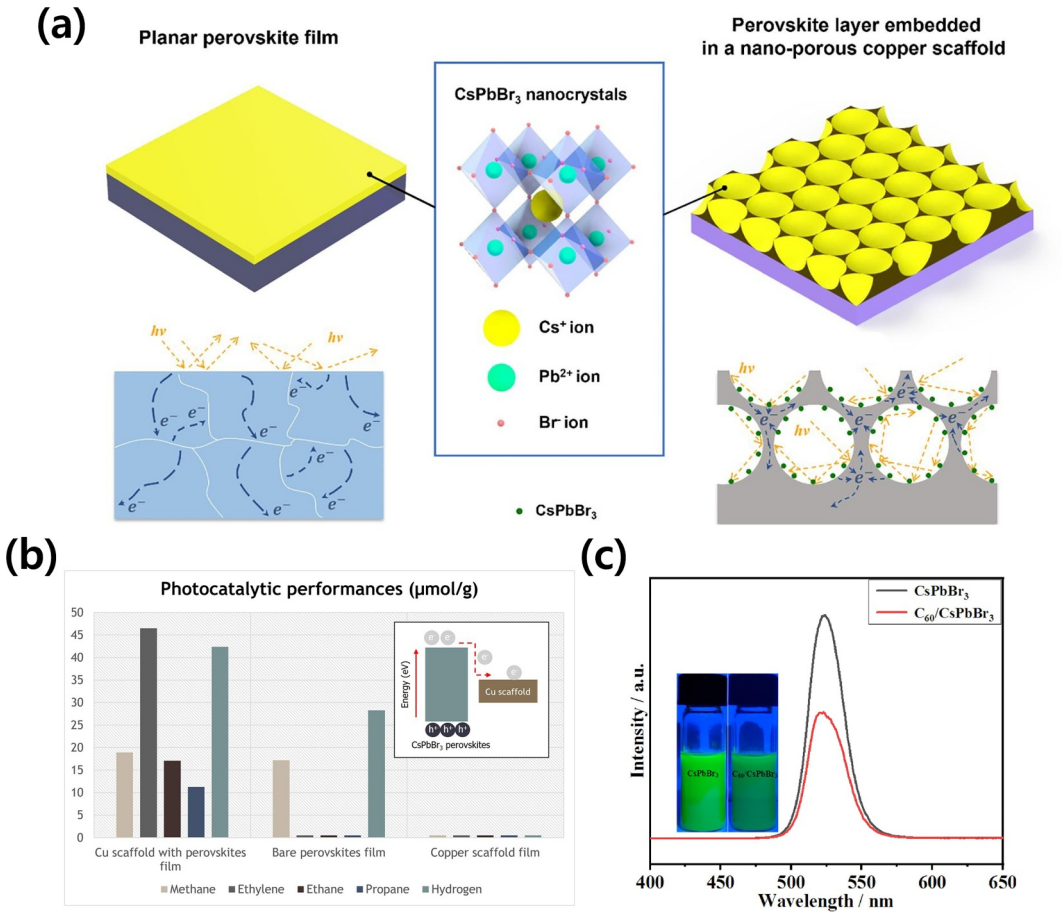


FIGURE 8 | Porous scaffold-supported perovskite photocatalysts. (a) Schematic comparison between a planar perovskite film and a porous copper-scaffold-embedded perovskite layer, illustrating enhanced light scattering and carrier migration in the porous architecture. (b) Comparison of photocatalytic product distributions for the porous-scaffold system and control samples. Reproduced with permission [104]. Copyright 2022, Elsevier. (c) PL spectra of pristine $CsPbBr_3$ and $C_{60}/CsPbBr_3$. Reproduced with permission [105]. Copyright 2021, Elsevier.

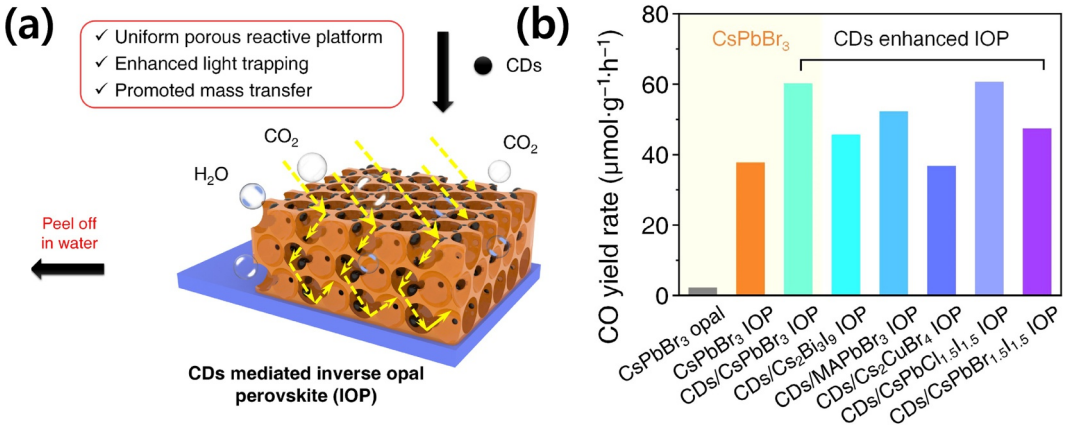


FIGURE 9 | (a) Schematic illustration of the CD-mediated IO perovskite film, showing the roles of the ordered porous structure in light trapping and mass transfer. (b) CO production rates of the IO systems with different compositions. Reproduced with permission [109]. Copyright 2025, Tsinghua University Press.

trend in photocatalysis involves exploiting structural asymmetry at the molecular and crystal-lattice levels to manipulate the quantum mechanical property of photoelectrons known as spin. Chiral materials possess inherently asymmetric helical or layered structures that cannot overlap with their mirror images. When electrons travel through such asymmetric frameworks, they can exhibit spin-selective transport, resulting in spin polarization. This phenomenon is termed the chirality-induced spin selectivity (CISS) effect [110].

In the photocatalytic CO_2 reduction, which requires sluggish multielectron-transfer processes, the exceedingly short lifetime

28359399, 0, Downloaded from https://onlinelibrary.wiley.com/doi/10.1002/ece2.70090 by Chung-Ang University, Wiley Online Library on [02/08/2026]. See the Terms and Conditions (https://onlinelibrary.wiley.com/terms-and-conditions) on Wiley Online Library for rules of use; OA articles are governed by the applicable Creative Commons License

of photogenerated charge carriers represents a significant limitation. However, when charge carriers are preferentially spin-polarized by a chiral structure, electron–hole recombination can be suppressed, possibly owing to spin-selective charge transport and a reduced probability of spin-allowed recombination [48]. Because spin-polarized electrons require additional energy and time to undergo a spin flip before recombination, the carrier lifetime is significantly extended. This section explores, through recent pioneering studies, how such crystallographic design of chiral materials can enhance the CO_2 photoreduction performance of perovskites.

As a representative study maximizing photocatalytic performance by inducing such spin polarization, Lin et al. reported a strategy for synthesizing Mn-doped $CsPbBr_3$ nanoparticles and applying an external magnetic field [111]. In this study, the magnetic Mn elements doped into the $CsPbBr_3$ lattice play a pivotal role in aligning the spin directions of photogenerated electrons. Particularly, when an external magnetic field is applied, the proportion of spin-polarized electrons sharply increases due to the Zeeman splitting effect (Figure 10a). This spin polarization may reduce the probability of spin-allowed recombination, thereby extending the carrier lifetime available for catalytic reactions. Consequently, under external magnetic fields of 0.1 and 0.3 T, the Mn-doped $CsPbBr_3$ photocatalyst enhanced the CO_2 reduction efficiency by 3.4-fold and 5.7-fold, respectively, compared to conditions without a magnetic field (Figure 10b).

Beyond the doping of magnetic elements, designing chiral 2D structures utilizing the spatial asymmetry of organic ligands has emerged as a core strategy for inducing spin polarization. Lin et al. successfully synthesized 2D RP-phase perovskites by incorporating chiral molecules, R/S-methylbenzylammonium bromide (MBA-Br), into $CsPbBr_3$ nanoplates [112]. This architecture manifests the aforementioned chirality-induced spin selectivity (CISS) effect, spontaneously aligning the spins of photogenerated carriers in a specific direction. Notably, when an external magnetic field is applied to this system, the Zeeman splitting phenomenon couples strongly with the spin selectivity of the chiral structure, creating a synergistic effect that maximizes the density of spin-polarized electrons. This highly ordered spin state strictly suppresses the nonradiative recombination of electrons and holes, thereby drastically extending the lifetime of the charge carriers. In practical photocatalytic CO_2 reduction evaluations, the chiral perovskite structure using (R)-MBA-Br exhibited a CO yield of 45.5 $\mu mol\ g^{-1}$ in the absence of a magnetic field, whereas its efficiency sharply escalated to 75.3 $\mu mol\ g^{-1}$ under a 0.3-T magnetic field (Figure 10c). This finding validates that the combination of asymmetric-ligand design and external magnetic fields represents a promising structural strategy for resolving kinetic bottlenecks in multielectron reactions.

6 | Plasmonic Enhancement and Metal–Perovskite Synergy

Plasmonic enhancement provides a distinct route for improving perovskite-based CO_2 photoreduction by coupling optical-field amplification with interfacial charge-transfer processes. When the size of metallic nanoparticles is significantly smaller than the wavelength of the incident light, the oscillating electric field of the light forces a collective coherent oscillation of the free

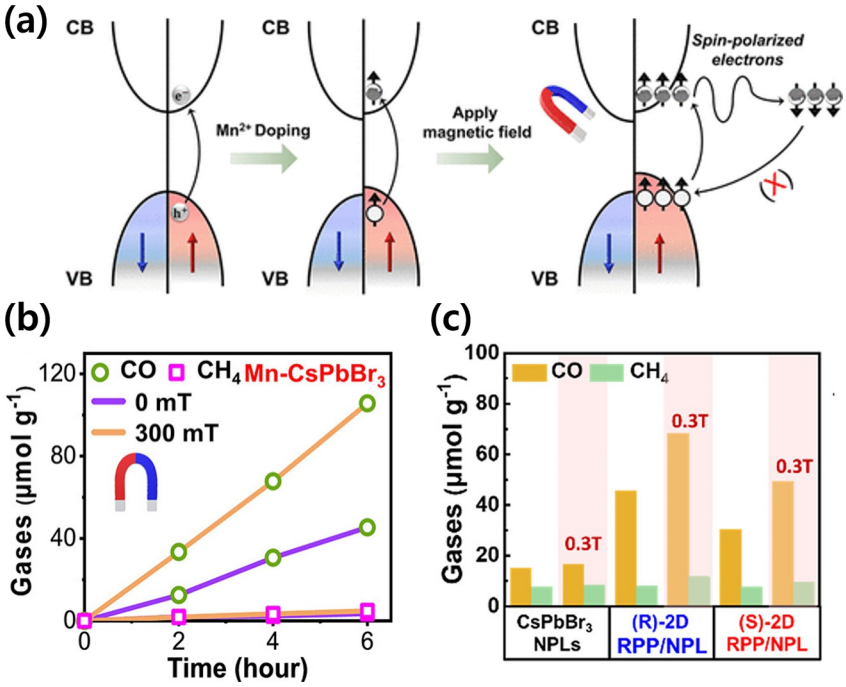


FIGURE 10 | Spin-selective strategies for suppressing charge recombination. (a) Schematic illustration of spin polarization induced by Mn doping and an external magnetic field, which suppresses electron–hole recombination. (b) Time-dependent CO and CH_4 production of Mn-doped $CsPbBr_3$ under different magnetic-field strengths. Reproduced with permission [111]. Copyright 2022, American Chemical Society. (c) Comparison of photocatalytic CO and CH_4 production in achiral and chiral 2D perovskite systems, showing the effect of CISS under a magnetic field. Reproduced with permission [112]. Copyright 2025, American Chemical Society.

28359399, 0, Downloaded from https://onlinelibrary.wiley.com/doi/10.1002/ece2.70090 by Chung-Ang University, Wiley Online Library on [02/08/2026]. See the Terms and Conditions (https://onlinelibrary.wiley.com/terms-and-conditions) on Wiley Online Library for rules of use; OA articles are governed by the applicable Creative Commons License

electrons present on the metal surface. Once the oscillation frequency of these free electrons matches the frequency of the incident light, a state of resonance is reached, causing the nanoparticles to strongly absorb and scatter light at specific wavelengths [113].

The fundamental reason why the LSPR phenomenon drastically improves photocatalytic performance lies in the decay process of the plasmon energy upon reaching the resonant state. To dissipate energy, plasmons primarily undergo two major pathways: radiative decay and nonradiative decay [114]. During the radiative decay process, the incident light is strongly scattered, forming a local electromagnetic field near the surface of the metal particles that is amplified by tens to hundreds of times compared to the original incident light. This phenomenon serves as the physical origin of the near-field enhancement effect. Conversely, during the nonradiative decay process, plasmon energy is directly transferred to the electronic system inside the metal through the Landau damping mechanism [115]. Electrons that absorb this massive amount of energy acquire extremely high kinetic energy, leaping well beyond the Fermi level, and are referred to as hot electrons. These high-energy hot electrons are rapidly injected into the surrounding medium or adjacent semiconductors, enabling energetically demanding chemical reactions that cannot occur under typical photoexcitation states.

In this section, plasmonic perovskite photocatalysts are classified according to their dominant enhancement pathway. First, near-field enhancement is discussed as an optical antenna effect that broadens light harvesting and intensifies local photoexcitation. Second, hot-electron injection across metal/perovskite interfaces is examined as a charge-transfer mechanism that can promote carrier utilization and suppress recombination. Finally, plasmonic metals are discussed as electron mediators in heterojunction and Z-scheme systems, in which their high conductivity and LSPR response synergistically regulate interfacial charge migration for CO_2 photoreduction.

6.1 | Near-Field Enhancement as an Optical Antenna Effect

Near-field enhancement represents the optical contribution of plasmonic metals to perovskite photocatalysis. When plasmonic nanoparticles are excited at their resonance frequency, the oscillating electrons generate an intensified local electromagnetic field near the metal surface. If perovskite domains are positioned within this near-field region, their effective absorption cross-section can be increased, leading to enhanced electron–hole pair generation even without directly changing the intrinsic bandgap of the perovskite [116]. In this sense, plasmonic nanoparticles can act as optical antennas that concentrate incident photons and extend the usable spectral range of the photocatalytic system. This mechanism should be distinguished from hot-electron injection because the primary role of the metal in near-field enhancement is to amplify local photoexcitation rather than directly transfer energetic carriers across the interface.

A representative example of this optical antenna effect is the 3DOM Au-$CsPbBr_3$ photocatalyst reported by Tang et al. [117]. In this system, Au nanoparticles were incorporated into a three-dimensionally ordered macroporous $CsPbBr_3$ framework (Figure 11a). The 3DOM perovskite skeleton first enhances photon utilization by inducing multiple scattering and extending the optical path length within the porous network. Simultaneously, Au nanoparticles generate an LSPR response that broadens the optical absorption of the composite. Notably, the Au-containing 3DOM $CsPbBr_3$ system showed enhanced light harvesting even in the wavelength region beyond 570 nm, where pristine $CsPbBr_3$ exhibits limited absorption (Figure 11b). This expanded optical response was accompanied by improved charge separation associated with metal–semiconductor interfacial band bending. As a result, the optimized 3DOM Au-$CsPbBr_3$ photocatalyst achieved an electron consumption rate of 38.0 $\mu mol\ g^{-1}\ h^{-1}$ for CO_2 reduction, corresponding to a 2.6-fold enhancement compared with bulk $CsPbBr_3$ (Figure 11c). This example demonstrates that combining ordered macroporous light scattering with plasmonic near-field amplification can effectively improve photon utilization in perovskite CO_2 photoreduction.

In addition to noble-metal plasmonic systems, more economical plasmonic components have also been explored. Wu et al. fabricated a Bi/$CsPbBr_3$ composite by growing Bi nanoparticles in situ on the surface of $CsPbBr_3$ [118]. The Bi nanoparticles exhibited an SPR response, thereby expanding the visible-light absorption capability of the photocatalytic system (Figure 11d). In addition to optical absorption enhancement, the plasmonic Bi component generated a photothermal effect under illumination, locally increasing the catalyst temperature and accelerating interfacial charge transfer and surface reaction kinetics. Coupled with band bending at the Bi/$CsPbBr_3$ interface, this optical–thermal synergy promoted charge separation and CO_2 reduction, giving a CO yield of 76.4 $\mu mol\ g^{-1}$ with a high CO selectivity of 97% (Figure 11e). This result suggests that plasmonic enhancement in perovskite photocatalysts can be extended beyond noble metals, providing a practical route to combine near-field light harvesting, photothermal acceleration, and interfacial charge regulation.

6.2 | Hot-Electron Injection Across Metal/Perovskite Interfaces

In contrast to near-field enhancement, which primarily amplifies local photoexcitation, plasmon-induced hot-electron injection directly contributes to interfacial charge transfer. When plasmonic metals undergo nonradiative decay, energetic hot electrons are generated above the Fermi level. If the metal is electronically coupled with a neighboring semiconductor, these hot electrons can be injected across the interface when their energy exceeds the interfacial barrier. In metal/perovskite systems, the resulting Schottky-type interface can promote directional electron transfer while suppressing back transfer, thereby prolonging charge lifetime and improving charge utilization for photocatalytic CO_2 reduction [114, 115]. A representative mechanistic example is the Au@CdS/$CsPbBr_3$ triple-heteronanocrystal system reported by Wan et al. [119]. Direct contact between plasmonic metals and perovskites can cause severe plasmon damping or interfacial instability. To overcome this issue, the authors introduced a thin CdS bridge between Au nanoparticles and $CsPbBr_3$. This nonepitaxial/epitaxial interfacial design preserved the LSPR response of Au while providing favorable energy alignment for hot-electron transfer from Au to $CsPbBr_3$ through CdS. Transient absorption spectroscopy revealed that the

28359399, 0, Downloaded from https://onlinelibrary.wiley.com/doi/10.1002/ece2.70090 by Chung-Ang University, Wiley Online Library on [02/08/2026]. See the Terms and Conditions (https://onlinelibrary.wiley.com/terms-and-conditions) on Wiley Online Library for rules of use; OA articles are governed by the applicable Creative Commons License

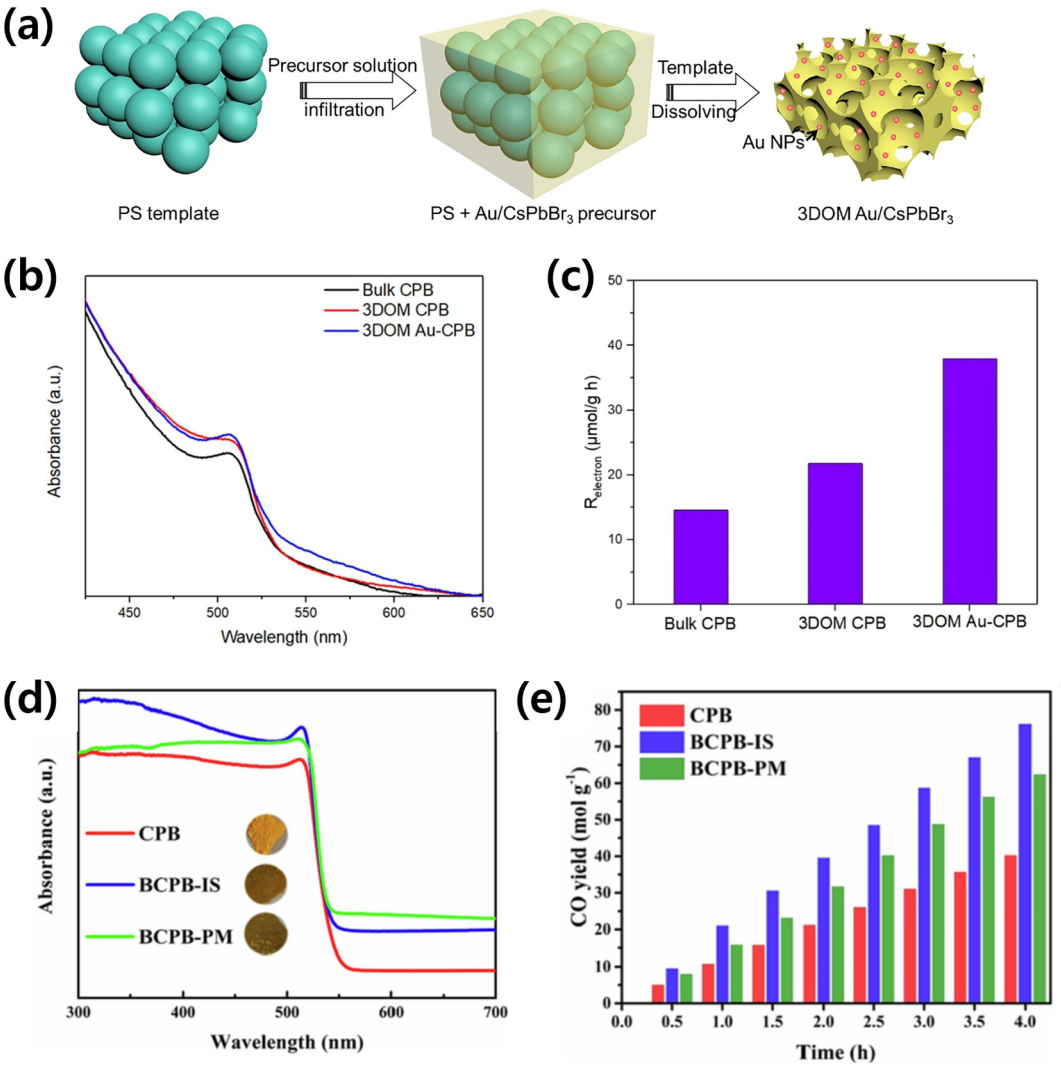


FIGURE 11 | (a) Schematic illustration of the fabrication of the 3DOM Au/$CsPbBr_3$ photocatalyst. (b) UV–Vis absorption spectra of bulk $CsPbBr_3$, 3DOM $CsPbBr_3$, and 3DOM Au/$CsPbBr_3$, showing the broadened optical response induced by the ordered architecture and Au nanoparticles. (c) Comparison of photocatalytic electron consumption rates. Reproduced with permission [117]. Copyright 2022, Chemical Engineering Journal. (d) Absorbance spectrum of Bi/$CsPbBr_3$. (e) CO yield of Bi/$CsPbBr_3$ samples. Reproduced with permission [118]. Copyright 2022, Elsevier.

extracted plasmon-induced hot electrons exhibited an ultralong lifetime on the nanosecond scale. Although this example is not itself a CO_2 photoreduction system, it clearly demonstrates how interfacial engineering can stabilize plasmon-excited electrons and enable efficient hot-electron injection into halide perovskites.

For CO_2 photoreduction, Liao et al. demonstrated a plasmonic $CsPbBr_3$-Au nanocomposite in which Au nanoparticles were anchored onto $CsPbBr_3$ nanocrystals using mercaptopropanoic acid as a molecular linker [120]. The intimate Au/perovskite interface forms a Schottky junction, allowing photoexcited electrons from $CsPbBr_3$ to migrate toward Au while suppressing their back transfer to the perovskite. This directional charge extraction reduces radiative recombination, as supported by the shortened photoluminescence lifetime after Au coupling. In this system, Au does not merely function as an optical antenna; it also acts as an electron-collecting site where separated charges can participate in surface reactions. As a result, the $CsPbBr_3$-Au nanocomposite achieved a CO_2 reduction yield of 47.7 μmol g^{-1}. This example highlights that rationally designed metal/perovskite Schottky interfaces can enhance photocatalytic activity by combining plasmonic excitation with directional charge transfer.

Overall, hot-electron injection differs from near-field enhancement in that the plasmonic metal directly participates in carrier transport rather than only amplifying the local optical field. Therefore, the key design parameters for this strategy are the interfacial barrier height, electronic coupling strength, metal–perovskite contact quality, and suppression of charge back transfer. These factors determine whether plasmon-generated energetic carriers can be effectively harvested for CO_2 reduction before thermalization or recombination.

6.3 | Plasmonic Mediator in Z-Scheme and Heterojunctions

Beyond near-field enhancement and hot-electron injection at single-metal/perovskite interfaces, plasmonic nanoparticles can also function as conductive mediators in multicomponent heterojunction systems. In this configuration, the metal component

28359399, 0, Downloaded from https://onlinelibrary.wiley.com/doi/10.1002/ece2.70090 by Chung-Ang University, Wiley Online Library on [02/08/2026]. See the Terms and Conditions (https://onlinelibrary.wiley.com/terms-and-conditions) on Wiley Online Library for rules of use; OA articles are governed by the applicable Creative Commons License

does not merely amplify local optical fields or inject hot carriers into an adjacent semiconductor. Instead, it provides an electron-transfer bridge that connects different photoactive components and regulates directional charge migration across the heterojunction. This mediator role is particularly important in Z-scheme or ternary heterojunction systems, where selective recombination of low-energy carriers and preservation of high-energy redox carriers must occur simultaneously. Because plasmonic metals possess high electrical conductivity and an LSPR response, they can combine charge mediation with enhanced visible-light utilization.

A representative example is the Ag/$CsPbBr_3$/g-C_3N_4 ternary heterojunction reported by Li et al. [121]. In this system, Ag nanoparticles were introduced between $CsPbBr_3$ nanocrystals and graphitic carbon nitride to construct an interfacial electron-transfer pathway for gas-phase CO_2 reduction. The Ag nanoparticles showed a distinct absorption feature near 530 nm, confirming their plasmonic contribution to the visible-light response (Figure 12a). More importantly, Ag acted as an electron mediator rather than a simple optical enhancer. Upon illumination, photogenerated electrons from $CsPbBr_3$ were rapidly transported through Ag nanoparticles toward g-C_3N_4, whereas the intimate Ag/g-C_3N_4 interface provided favorable sites for CO_2 adsorption and reduction. This directional charge migration suppressed nonradiative recombination and allowed spatially separated electrons to participate efficiently in CO_2-to-CO conversion (Figure 12b). As a result, the Ag/$CsPbBr_3$/g-C_3N_4 ternary photocatalyst achieved a CO production rate of 19.49 μmol g^{-1} h^{-1} with nearly 100% product selectivity.

This example highlights the distinct function of plasmonic mediators compared with the systems discussed in Sections 6.1 and 6.2. In near-field enhancement, the plasmonic metal primarily acts as an optical antenna, whereas in hot-electron injection, it directly supplies energetic carriers across a metal/semiconductor interface. In mediator-type heterojunctions, however, the metal serves as an interfacial charge-transfer channel that couples multiple semiconductors and guides electron flow. Therefore, the effectiveness of plasmonic mediator systems depends on the spatial arrangement of the metal nanoparticles, the contact quality with adjacent semiconductors, and the alignment of reaction sites with the direction of charge migration. Rationally designing such ternary interfaces offers a promising route for integrating plasmonic light harvesting with interfacial charge control in perovskite-based CO_2 photoreduction. Table 1 summarizes the representative perovskite-based photocatalytic systems covered in this review, highlighting their key design features and photocatalytic performances.

7 | Conclusions and Outlook

Halide perovskites have emerged as promising photocatalytic materials for CO_2 reduction owing to their strong visible-light absorption, tunable electronic structures, and favorable charge-transport properties. However, their practical performance is still limited by charge recombination, inefficient interfacial charge transfer, instability under polar reaction environments, and insufficient control over product selectivity. In this review, we reorganized recent progress in perovskite-based CO_2 photoreduction according to four interconnected design principles: electronic structure engineering, interfacial charge-transfer design, structural optical and spin-selective engineering, and plasmonic metal–semiconductor synergy.

Electronic structure engineering provides the intrinsic basis for photocatalytic activity by tuning bandgaps, band-edge positions, orbital hybridization, crystallographic dimensionality, and defect states. Compositional tuning and dimensionality control regulate light absorption and redox energetics, whereas defect passivation and controlled defect utilization must be carefully distinguished to suppress detrimental recombination centers while preserving beneficial shallow states for charge transfer and intermediate activation.

Interfacial design further determines whether photogenerated carriers can be efficiently separated and utilized. Type-II heterojunctions promote spatial charge separation, whereas Z-scheme and S-scheme systems preserve stronger redox potentials by selectively removing low-energy carriers. Therefore, rational band alignment, Fermi-level modulation, and built-in electric fields are essential for balancing charge separation with the thermodynamic driving force required for multielectron CO_2 reduction.

Structural optical engineering and plasmonic enhancement provide additional routes to improve photon utilization and reaction kinetics. Porous scaffolds, hollow architectures, inverse opals, and chiral structures can enhance light trapping, CO_2 diffusion, carrier transport, and spin-selective charge separation.

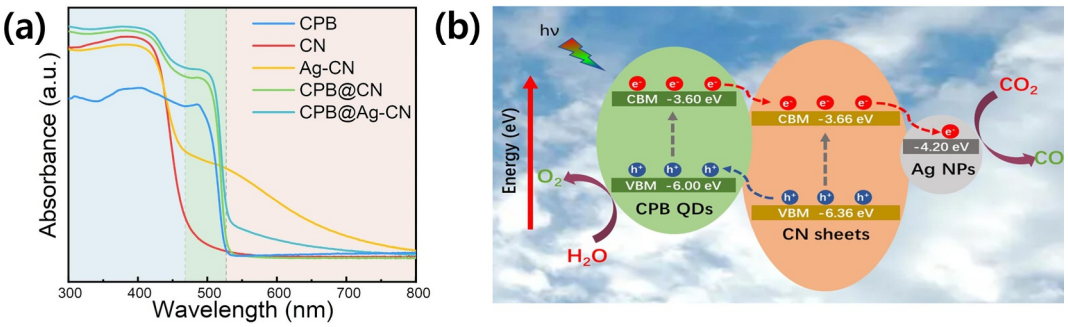


FIGURE 12 | (a) UV–Vis absorption spectra of the individual components and Ag-containing composites, demonstrating the enhanced visible-light response after plasmonic integration. (b) Schematic illustration of the Ag/$CsPbBr_3$/g-C_3N_4 ternary heterojunction, showing Ag-mediated electron transfer for efficient CO_2 reduction. Reproduced with permission [121]. Copyright 2025, Ji Hua Laboratory.

28359399, 0, Downloaded from https://onlinelibrary.wiley.com/doi/10.1002/ece2.70090 by Chung-Ang University, Wiley Online Library on [02/08/2026]. See the Terms and Conditions (https://onlinelibrary.wiley.com/terms-and-conditions) on Wiley Online Library for rules of use; OA articles are governed by the applicable Creative Commons License

TABLE 1 | Photocatalytic performances of perovskite-based systems discussed in this review.

Strategy	Representative system	Performance	Key feature	Ref.
Electronic structure engineering/ compositional tuning	$Cs_3Sb_2Cl_4Br_5$	CH_4: 4.92 μmol g^{-1} after 6 h	X-site Cl/Br mixing	[73]
Electronic structure engineering/B-site alloying	$Cs_3Sb_{0.5}Bi_{1.5}Cl_4Br_5$	CH_4: 6.28 μmol g^{-1} after 6 h	Bi-mediated B-site alloying	[74]
Electronic structure engineering/ crystallographic dimensionality	$Cs_5Pb_4Br_{13}$/RGO (n = 4 IRPP)	Total CO_2 reduction products: 81.39 μmol g^{-1}; n = 3 counterpart: 54.82 μmol g^{-1}	Relaxed quantum confinement	[84]
Electronic structure engineering/ crystallographic dimensionality	$Cs_4CuSb_2Cl_{12}$	CO: 223 μmol g^{-1}; CH_4: 74 μmol g^{-1} over 3 h	Layered direct-bandgap structure	[85]
Electronic structure engineering/ dopant-mediated charge control	Mn-doped $CsPb(Br/Cl)_3$	CO: 1917 μmol g^{-1}; CH_4: 82 μmol g^{-1}	Mn-mediated charge separation	[87]
Electronic structure engineering/ surface functionalization and vacancy control	FcA-modified, Br-vacancy-rich $CsPbBr_3$	> 2-fold enhancement compared with pristine $CsPbBr_3$	FcA-assisted vacancy control	[88]
Electronic structure engineering/ vacancy engineering	$Cs_2NaBiCl_6$-G	CO: 30.22 μmol g^{-1} h^{-1}	Cl-vacancy defect levels	[89]
Electronic structure engineering/ lattice-strain engineering	$CsPb_{0.9}Cu_{0.1}Br_3$	CO: 69.75 μmol g^{-1}; CH_4: 25.84 μmol g^{-1} within 3 h; CO selectivity: 74%	Cu-induced shallow traps	[90]
Interfacial design/Type-II heterojunction	$CsPbBr_3$/CdSe	CO: 115.26 μmol g^{-1}; 4.6-fold higher than pristine $CsPbBr_3$	0D/0D Type-II interface	[92]
Interfacial design/Type-II polymer–perovskite heterojunction	P3HT/$CsPbBr_3$	CO: 145.45 μmol g^{-1} h^{-1}; CH_4: 23.05 μmol g^{-1} h^{-1}; electron consumption: 475.3 μmol g^{-1} h^{-1}	P3HT hole extraction layer	[93]
Interfacial design/Z-scheme heterojunction	$Cs_2AgBiBr_6$@g-C_3N_4-82%	CH_4 selectivity > 70%; total activity 16-fold and 10-fold higher than CABB and g-C_3N_4	Z-scheme CH_4 selectivity	[94]
Interfacial design/S-scheme heterojunction	T-101/$CsPbBr_3$	CO: 12.5 μmol h^{-1}; CO selectivity: 90.2%; 15.6-fold higher than pristine T-101	Facet-tuned S-scheme field	[95]
Structural optical engineering/hollow architecture	$CsPbBr_3$/Co_3O_4 hollow nanocage (CPBCO)	CO: 55.82 μmol g^{-1} h^{-1}; CH_4: 5.98 μmol g^{-1} h^{-1}	Hollow p-n nanocage	[100]
Structural optical engineering/hollow lead-free perovskite	H-$Cs_3Sb_2Br_9$ + dinuclear Co complex	CO: 15 010.4 μmol g^{-1} over 8 h; 28-fold higher than solid nanocrystals	Hollow light-trapping nanosphere	[101]
Structural optical engineering/ multishell hollow heterostructure	TiO_2/$Cs_3Bi_2I_9$/g-C_3N_4	CO: 120.6 μmol g^{-1} h^{-1}; 3.1-fold higher than pristine $Cs_3Bi_2I_9$; stable for 100 h	Multishell spatial separation	[102]
Structural optical engineering/3D porous aerogel	$CsPbBr_3$/$Ti_3C_2T_x$ MXene aerogel	Electron consumption: 112.6 μmol g^{-1} h^{-1}	MXene 3D porous scaffold	[103]
Structural optical engineering/porous scaffold and product selectivity	$CsPbBr_3$ embedded in porous Cu scaffold	Product selectivity shifts from C1 products toward C_2H_4 and C_2H_6	Porous Cu C–C coupling sites	[104]
Structural optical engineering/ molecular support and electron acceptor	C_{60}/$CsPbBr_3$	Enhanced CO_2 photoreduction activity compared with pristine $CsPbBr_3$	C_{60} electron-acceptor support	[105]
Structural optical engineering/2D support scaffold	$CsPbBr_3$/NiAl-LDH	3.7-fold enhancement compared with pristine $CsPbBr_3$	LDH stabilization scaffold	[106]

(Continues)

28359399, 0, Downloaded from https://onlinelibrary.wiley.com/doi/10.1002/ece2.70090 by Chung-Ang University, Wiley Online Library on [02/08/2026]. See the Terms and Conditions (https://onlinelibrary.wiley.com/terms-and-conditions) on Wiley Online Library for rules of use; OA articles are governed by the applicable Creative Commons License

TABLE 1 | (Continued)

Strategy	Representative system	Performance	Key feature	Ref.
Structural optical engineering/inverse-opal photonic structure	CDs/IO-$CsPbBr_3$	CO: 60.25 μmol g^{-1} h^{-1}; 15.6-fold higher than conventional $CsPbBr_3$	Carbon-dot-bridged inverse opal	[109]
Structural optical and spin-selective engineering/magnetic-field-assisted spin polarization	Mn-doped $CsPbBr_3$ + external magnetic field	3.4-fold enhancement at 0.1 T; 5.7-fold enhancement at 0.3 T	Magnetic spin polarization	[111]
Structural optical and spin-selective engineering/chiral 2D perovskite	(R)-MBA-Br-based chiral 2D perovskite	CO: 45.5 μmol g^{-1} at 0 T; 75.3 μmol g^{-1} at 0.3 T	Chiral CISS effect	[112]
Plasmonic enhancement/near-field optical antenna	3DOM Au-$CsPbBr_3$	Electron consumption: 38.0 μmol g^{-1} h^{-1}; 2.6-fold higher than bulk $CsPbBr_3$	3DOM Au LSPR antenna	[117]
Plasmonic enhancement/ SPR–photothermal synergy	Bi/$CsPbBr_3$	CO: 76.4 μmol g^{-1}; CO selectivity: 97%	Bi SPR-photothermal effect	[118]
Plasmonic enhancement/Schottky junction	CsPbBr3-Au linked by mercaptopropanoic acid	CO_2 reduction yield: 47.7 μmol g^{-1}	Au Schottky electron extraction	[120]
Plasmonic enhancement/plasmonic mediator in ternary heterojunction	Ag/CsPbBr3/g-C3N4	CO: 19.49 μmol g^{-1} h^{-1}; nearly 100% CO selectivity	Ag-mediated electron transfer	[121]

Meanwhile, plasmonic metals can act through distinct mechanisms, including near-field optical amplification, hot-electron injection, and charge mediation in heterojunction systems. Clearly distinguishing these pathways is critical for designing effective plasmonic perovskite photocatalysts.

Despite these advances, several challenges remain. First, long-term stability under moisture, oxygen, polar solvents, and continuous illumination must be improved through protective architectures that simultaneously allow charge transfer and reactant diffusion. Recent core–shell, multishell, MOF-encapsulated, and carbon-mediated structures have shown that physical protection can be combined with interfacial charge extraction and CO_2 adsorption enhancement. However, future protective layers should be designed not merely as passive barriers but as multifunctional interfaces that regulate ion migration, suppress phase decomposition, and maintain catalytic accessibility during long-term operation.

Second, lead-free perovskites based on Bi, Sb, Sn, Ag, and Cu should be further developed to address toxicity concerns. Recent Sb- and Bi-based halide perovskites have demonstrated that compositional tuning, B-site alloying, vacancy control, and heterojunction formation can improve visible-light absorption and CO_2 reduction activity. Nevertheless, many lead-free systems still suffer from indirect bandgaps, poor carrier mobility, and limited surface reactivity compared with Pb-based counterparts. Therefore, future studies should combine lead-free composition design with defect regulation, interfacial charge-transfer engineering, and optical light-management strategies.

Third, future studies should combine operando spectroscopy, isotope labeling, transient spectroscopy, surface photovoltage analysis, and theoretical calculations to verify charge-transfer pathways and reaction intermediates. Assigning Type-II, Z-scheme, S-scheme, or plasmon-mediated mechanisms only from band diagrams or PL quenching is insufficient. More rigorous evidence is needed to correlate band alignment, carrier migration, intermediate formation, and final product distribution under actual reaction conditions.

Finally, more attention should be paid to product selectivity, especially the selective formation of CH_4, liquid fuels, and C^{2+} products. Current perovskite photocatalysts mainly produce CO or CH_4, but recent results suggest that interfacial architecture and catalytic active sites can redirect reaction pathways toward deeper reduction or C–C coupling. Future catalyst design should therefore focus on stabilizing key intermediates such as *COOH, *CO, and *CHO while introducing active sites that promote multielectron/proton transfer. Overall, future perovskite photocatalysts should be designed as integrated systems that simultaneously optimize light harvesting, charge separation, surface catalysis, mass transport, and structural durability.

Author Contributions

Jaemin Jeong: writing – original draft, investigation, **Myeongjin Seol:** resources, investigation. **Sang Hyun Ahn:** writing – review and editing. **Soo Young Kim:** supervision, writing – review and editing, funding acquisition.

Funding

This research was supported by the NRF funded by the Korean government (RS-2022-NR068226; RS-2025-00558945).

Ethics Statement

The authors have nothing to report.

28359399, 0, Downloaded from https://onlinelibrary.wiley.com/doi/10.1002/ece2.70090 by Chung-Ang University, Wiley Online Library on [02/08/2026]. See the Terms and Conditions (https://onlinelibrary.wiley.com/terms-and-conditions) on Wiley Online Library for rules of use; OA articles are governed by the applicable Creative Commons License

Consent

The authors have nothing to report.

Conflicts of Interest

The authors declare no conflicts of interest.

Data Availability Statement

Data sharing is not applicable to this article as no datasets were generated or analyzed during this study.

References

1. Y. Zhou, Z. Wang, L. Huang, et al., "Engineering 2D Photocatalysts Toward Carbon Dioxide Reduction," *Advanced Energy Materials* 11, no. 8 (2021): 2003159, https://doi.org/10.1002/aenm.202003159.

2. D. C. Liu, Z. M. Luo, B. M. Aramburu-Troselj, F. Ma, and J. W. Wang, "Cobalt-Based Tripodal Complexes as Molecular Catalysts for Photocatalytic CO_2 Reduction," *Chemical Communications* 59, no. 99 (2023): 14626–14635, https://doi.org/10.1039/d3cc04759h.

3. M. N. Chu, Y. Li, K. Cui, et al., "Enhanced Photocatalytic Reduction of Carbon Dioxide Into Carbon Monoxide by Electric Field Generation and Defect Engineering in TiO," *Environmental Chemistry Letters* 20, no. 2 (2022): 999–1007, https://doi.org/10.1007/s10311-021-01381-x.

4. J. W. Wei, S. M. Zhang, J. L. Sun, et al., "Z-scheme CoAl-Layered Double Hydroxide/Indium Vanadate Heterojunction for Enhanced and Highly Selective Photocatalytic Reduction of Carbon Dioxide to Carbon Monoxide," *Journal of Colloid and Interface Science* 629 (2023): 92–102, https://doi.org/10.1016/j.jcis.2022.08.148.

5. J. H. Kim, J. Kim, J. Ma, et al., "Spontaneous Metal-Chelation Strategy for Highly Dense Ni Single-Atom Catalysts With Asymmetric Coordination in CO_2 Electroreduction," *Small* 21, no. 5 (2025): 2409481, https://doi.org/10.1002/smll.202409481.

6. J. Ma, W. Lee, J. H. Kim, et al., "Leveraging the Intermetal Distance in Dual-Atom Catalysts: Revealing Optimized Synergistic Interactions for CO_2 Electroreduction," *ACS Nano* 19 (2025): 18698–18707, https://doi.org/10.1021/acsnano.5c03160.

7. S. Mehregan, F. Hayati, M. Mehregan, et al., "Exploring the Visible Light-Assisted Conversion of CO_2 into Methane and Methanol, Using Direct Z-Scheme TiO_2@g-C_3N_4 Nanosheets: Synthesis and Photocatalytic Performance," *Environmental Science and Pollution Research* 29, no. 49 (2022): 74951–74966, https://doi.org/10.1007/s11356-022-21048-6.

8. S. M. Liang, Y. J. Chen, W. Han, Y. Z. Jiao, W. Li, and G. H. Tian, "Hierarchical S-Scheme Titanium dioxide@cobalt-nickel Based Metal-Organic Framework Nanotube Photocatalyst for Selective Carbon Dioxide Photoreduction to Methane," *Journal of Colloid and Interface Science* 630 (2023): 11–22, https://doi.org/10.1016/j.jcis.2022.09.115.

9. J. Zhao, Y. Ma, Z. Tong, et al., "Co_3O_4@NH_2-MIL-125(Ti) Nanocomposites With Crystal Facet Engineering for Enhanced Photocatalytic CO_2 Reduction," *Journal of Environmental Chemical Engineering* 13, no. 2 (2025): 115693, https://doi.org/10.1016/j.jece.2025.115693.

10. X.-M. Cheng, X.-Y. Zhang, X.-Y. Dao, S.-Q. Wang, J. Zhao, and W.-Y. Sun, "High-Index Facets Exposed on Metal-Organic Framework for Boosting Photocatalytic Carbon Dioxide Reduction," *Chemical Engineering Journal* 431 (2022): 134125, https://doi.org/10.1016/j.cej.2021.134125.

11. S. Yu, P. Lv, P. Xue, et al., "Light-Driven Enzymatic Nanosystem for Highly Selective Production of Formic Acid From CO_2," *Chemical Engineering Journal* 420 (2021): 127649, https://doi.org/10.1016/j.cej.2020.127649.

12. P. Y. Zhang, J. D. Hu, Y. B. Shen, et al., "Photoenzymatic Catalytic Cascade System of a Pyromellitic Diimide/g-C_3N_4 Heterojunction to Efficiently Regenerate NADH for Highly Selective CO Reduction Toward Formic Acid," *Acs Applied Materials & Interfaces* 13, no. 39 (2021): 46650–46658, https://doi.org/10.1021/acsami.1c13167.

13. A. R. A. Astuti, W. H. Saputera, D. Ariono, I. G. Wenten, and D. Sasongko, "Enhancing CO Capture and Conversion to Formic Acid via a Membrane-Photocatalytic Hybrid System With ZnO-ZnS Heterojunction Catalyst," *ACS Omega* 10, no. 6 (2025): 5563–5573, https://doi.org/10.1021/acsomega.4c08249.

14. W. Zhang, Q. Zhou, N. Li, and M. Li, "Enhanced Photocatalytic Reduction of CO_2 into CH_4 Over N, Eu Co-Doped TiO_2: Insight into the Synergistic Effect of N and Eu," *Applied Catalysis A: General* 650 (2023): 118977, https://doi.org/10.1016/j.apcata.2022.118977.

15. Y. S. Lai, C. T. Cheng, J. L. Liou, J. M. Jehng, and Y. M. Dai, "The ZnO-Au-Titanium Oxide Nanotubes (TiNTs) Composites Photocatalysts for CO_2 Reduction Application," *Ceramics International* 47, no. 21 (2021): 30020–30029, https://doi.org/10.1016/j.ceramint.2021.07.177.

16. S. Singh, R. Kumar, K. K. Pant, S. Kumar, D. Joshi, and P. Biswas, "Mechanistic Exploration in Controlling the Product Selectivity via Metals in TiO_2 for Photocatalytic Carbon Dioxide Reduction," *Applied Catalysis B: Environment and Energy* 352 (2024): 124054, https://doi.org/10.1016/j.apcatb.2024.124054.

17. A. R. A. Astuti, D. Ariono, I. G. Wenten, D. Sasongko, W. H. Saputera, and K. A. Kurnia, "Mechanistic Insights into CO_2 Photoreduction to Formic Acid Using ZnO Catalysts," *Chemical Engineering Research and Design* 218 (2025): 664–673, https://doi.org/10.1016/j.cherd.2025.05.011.

18. X. Liu, Y. J. Chen, Q. Wang, L. G. Li, L. Z. Du, and G. H. Tian, "Improved Charge Separation and Carbon Dioxide Photoreduction Performance of Surface Oxygen Vacancy-enriched Zinc Ferrite@Titanium Dioxide Hollow Nanospheres With Spatially Separated Co-catalysts," *Journal of Colloid and Interface Science* 599 (2021): 1–11, https://doi.org/10.1016/j.jcis.2021.04.104.

19. A. R. A. Astuti, W. H. Saputera, D. Ariono, I. G. Wenten, and D. Sasongko, "Membrane Contactor-Photocatalytic Hybrid System for Carbon Dioxide Capture and Conversion to Formic Acid," *Results in Engineering* 22 (2024): 102085, https://doi.org/10.1016/j.rineng.2024.102085.

20. Y. B. Lim and S. Y. Kim, "Recent Advances in Buffer Layer Engineering for Performance Enhancement in Inverted Perovskite Solar Cells: Material-Based Classification," *Transactions on Electrical and Electronic Materials* 26 (2025): 487, https://doi.org/10.1007/s42341-025-00652-6.

21. W. J. Jang, P. J. Park, J. Ma, and S. Y. Kim, "Engineering Perovskite Solar Cells for Photovoltaic and Photoelectrochemical Systems: Strategies for Enhancing Efficiency and Stability," *Chemical Communications* 61, no. 45 (2025): 8137–8156, https://doi.org/10.1039/d5cc01338k.

22. B. Kang and F. Yan, "Emerging Strategies for the Large-Scale Fabrication of Perovskite Solar Modules: From Design to Process," *Energy & Environmental Science* 18, no. 9 (2025): 3917–3954, https://doi.org/10.1039/d4ee05613b.

23. H. Huang, D. Verhaeghe, B. Weng, et al., "Metal Halide Perovskite Based Heterojunction Photocatalysts," *Angewandte Chemie International Edition* 61, no. 24 (2022): e202203261, https://doi.org/10.1002/anie.202203261.

24. J. Maes, L. Balcaen, E. Drijvers, et al., "Light Absorption Coefficient of $CsPbBr_3$ Perovskite Nanocrystals," *Journal of Physical Chemistry Letters* 9, no. 11 (2018): 3093–3097, https://doi.org/10.1021/acs.jpclett.8b01065.

25. A. K Al-Mousoi, M. K. Mohammed, S. Q. Salih, et al., "Comparative Study of the Correlation Between Diffusion Length of Charge Carriers

28359399, 0, Downloaded from https://onlinelibrary.wiley.com/doi/10.1002/ece2.70090 by Chung-Ang University, Wiley Online Library on [02/08/2026]. See the Terms and Conditions (https://onlinelibrary.wiley.com/terms-and-conditions) on Wiley Online Library for rules of use; OA articles are governed by the applicable Creative Commons License

and the Performance of $CsSnGeI_3$ Perovskite Solar Cells," *Energy & Fuels* 36, no. 23 (2022): 14403–14410, https://doi.org/10.1021/acs.energyfuels.2c03390.

26. S. Lee, H. J. Jo, S. M. Han, Y. J. Kim, and S. Y. Kim, "Recent Advances in Ligand Engineering for Stable Halide Perovskite Light-Emitting Diodes," *Electronic Materials Letters* 21, no. 5 (2025): 633–649, https://doi.org/10.1007/s13391-025-00587-3.

27. S. Y. Hong, D. Y. Oh, and S. J. Oh, "Quantum Dot-Based Infrared Photodiodes and Image Sensors," *Transactions on Electrical and Electronic Materials* 27, no. 1 (2026): 6–22, https://doi.org/10.1007/s42341-025-00679-9.

28. N. Ahn and M. Choi, "Towards Long-Term Stable Perovskite Solar Cells: Degradation Mechanisms and Stabilization Techniques," *Advanced Science* 11, no. 4 (2024): 2306110, https://doi.org/10.1002/advs.202306110.

29. D. Chen, K. Xu, M. Yang, et al., "Surface Chemistry Engineering Enables Polar Solvent Resistant and Highly Emissive Perovskite Nanocrystals for Multifunctional Applications," *Chemical Engineering Journal* 471 (2023): 144848, https://doi.org/10.1016/j.cej.2023.144848.

30. J. Y. Loh, A. Mohan, A. G. Flood, G. A. Ozin, and N. P. Kherani, "Waveguide Photoreactor Enhances Solar Fuels Photon Utilization Towards Maximal Optoelectronic–Photocatalytic Synergy," *Nature Communications* 12, no. 1 (2021): 402, https://doi.org/10.1038/s41467-020-20613-2.

31. C. R. Dong, Y. Wang, K. Zhang, and H. Zeng, "Halide Perovskite Materials as Light Harvesters for Solar Energy Conversion," *Energy* 2, no. 1 (2020): 100026, https://doi.org/10.1016/j.enchem.2020.100026.

32. A. L. Linsebigler, G. Lu, and J. T. Yates Jr, "Photocatalysis on TiO_2 Surfaces: Principles, Mechanisms, and Selected Results," *Chemical Reviews* 95, no. 3 (1995): 735–758, https://doi.org/10.1021/cr00035a013.

33. C. M. Proctor, M. Kuik, and T.-Q. Nguyen, "Charge Carrier Recombination in Organic Solar Cells," *Progress in Polymer Science* 38, no. 12 (2013): 1941–1960, https://doi.org/10.1016/j.progpolymsci.2013.08.008.

34. R. D. Adhikari, M. J. Patel, H. Baishya, et al., "Decoding Recombination Dynamics in Perovskite Solar Cells: An In-Depth Critical Review," *Chemical Society Reviews* 54, no. 8 (2025): 3962–4034, https://doi.org/10.1039/d4cs01231c.

35. Q. Guo, J.-D. Zhang, J. Li, and X. Feng, "Solar-Driven Redox Reactions With Metal Halide Perovskites Heterogeneous Structures," *Nano-Micro Letters* 18, no. 1 (2026): 49, https://doi.org/10.1007/s40820-025-01886-y.

36. E. M. Hutter, M. C. Gélvez-Rueda, A. Osherov, et al., "Direct–Indirect Character of the Bandgap in Methylammonium Lead Iodide Perovskite," *Nature Materials* 16, no. 1 (2017): 115–120, https://doi.org/10.1038/nmat4765.

37. J. Xu, C. C. Boyd, Z. J. Yu, et al., "Triple-Halide Wide–Band Gap Perovskites With Suppressed Phase Segregation for Efficient Tandems," *Science* 367, no. 6482 (2020): 1097–1104, https://doi.org/10.1126/science.aaz5074.

38. A. Sadhanala, S. Ahmad, B. Zhao, et al., "Blue-Green Color Tunable Solution Processable Organolead Chloride–Bromide Mixed Halide Perovskites for Optoelectronic Applications," *Nano Letters* 15, no. 9 (2015): 6095–6101, https://doi.org/10.1021/acs.nanolett.5b02369.

39. S. A. Kulkarni, T. Baikie, P. P. Boix, N. Yantara, N. Mathews, and S. Mhaisalkar, "Band-Gap Tuning of Lead Halide Perovskites Using a Sequential Deposition Process," *Journal of Materials Chemistry A* 2, no. 24 (2014): 9221–9225, https://doi.org/10.1039/c4ta00435c.

40. J.-W. Lee, S. Tan, S. I. Seok, Y. Yang, and N.-G. Park, "Rethinking the A Cation in Halide Perovskites," *Science* 375, no. 6583 (2022): eabj1186, https://doi.org/10.1126/science.abj1186.

41. G. E. Eperon, S. D. Stranks, C. Menelaou, M. B. Johnston, L. M. Herz, and H. J. Snaith, "Formamidinium Lead Trihalide: A Broadly Tunable Perovskite for Efficient Planar Heterojunction Solar Cells," *Energy & Environmental Science* 7, no. 3 (2014): 982–988, https://doi.org/10.1039/c3ee43822h.

42. A. Amat, E. Mosconi, E. Ronca, et al., "Cation-Induced Band-Gap Tuning in Organohalide Perovskites: Interplay of Spin–Orbit Coupling and Octahedra Tilting," *Nano Letters* 14, no. 6 (2014): 3608–3616, https://doi.org/10.1021/nl5012992.

43. N. K. Noel, S. D. Stranks, A. Abate, et al., "Lead-Free Organic–Inorganic Tin Halide Perovskites for Photovoltaic Applications," *Energy & Environmental Science* 7, no. 9 (2014): 3061–3068, https://doi.org/10.1039/c4ee01076k.

44. W. Liao, D. Zhao, Y. Yu, et al., "Fabrication of Efficient Low-Bandgap Perovskite Solar Cells by Combining Formamidinium Tin Iodide With Methylammonium Lead Iodide," *Journal of the American Chemical Society* 138, no. 38 (2016): 12360–12363, https://doi.org/10.1021/jacs.6b08337.

45. S. D. Stranks, G. E. Eperon, G. Grancini, et al., "Electron-Hole Diffusion Lengths Exceeding 1 Micrometer in an Organometal Trihalide Perovskite Absorber," *Science* 342, no. 6156 (2013): 341–344, https://doi.org/10.1126/science.1243982.

46. C. Wehrenfennig, M. Liu, H. J. Snaith, M. B. Johnston, and L. M. Herz, "Charge-Carrier Dynamics in Vapour-Deposited Films of the Organolead Halide Perovskite $CH_3NH_3PbI_{3-x}Cl_x$," *Energy & Environmental Science* 7 (2014): 2269–2275, https://doi.org/10.1039/c4ee01358a.

47. L. M. Herz, "Charge-Carrier Mobilities in Metal Halide Perovskites: Fundamental Mechanisms and Limits," *ACS Energy Letters* 2, no. 7 (2017): 1539–1548, https://doi.org/10.1021/acsenergylett.7b00276.

48. S. He, Y. Chen, J. Fang, Y. Liu, and Z. Lin, "Optimizing Photocatalysis via Electron Spin Control," *Chemical Society Reviews* 54, no. 5 (2025): 2154–2187, https://doi.org/10.1039/D4CS00317A.

49. K. C. Harper, E. G. Moschetta, S. V. Bordawekar, and S. J. Wittenberger, "A Laser Driven Flow Chemistry Platform for Scaling Photochemical Reactions With Visible Light," *ACS Central Science* 5, no. 1 (2019): 109–115, https://doi.org/10.1021/acscentsci.8b00728.

50. M. Vezzoli, T. Farrell, A. Baker, S. Psaltis, W. N. Martens, and J. M. Bell, "Optimal Catalyst Thickness in Titanium Dioxide Fixed Film Reactors: Mathematical Modelling and Experimental Validation," *Chemical Engineering Journal* 234 (2013): 57–65, https://doi.org/10.1016/j.cej.2013.08.049.

51. A. R. Zanatta, "The Shockley–Queisser Limit and the Conversion Efficiency of Silicon-Based Solar Cells," *Results in Optics* 9 (2022): 100320, https://doi.org/10.1016/j.rio.2022.100320.

52. M. H. Miah, M. U. Khandaker, M. B. Rahman, M. Nur-E-Alam, and M. A. Islam, "Band Gap Tuning of Perovskite Solar Cells for Enhancing the Efficiency and Stability: Issues and Prospects," *RSC Advances* 14, no. 23 (2024): 15876–15906, https://doi.org/10.1039/d4ra01640h.

53. S. Wei, X. Xia, S. Bi, et al., "Metal–Insulator–Semiconductor Photoelectrodes for Enhanced Photoelectrochemical Water Splitting," *Chemical Society Reviews* 53, no. 13 (2024): 6860–6916, https://doi.org/10.1039/d3cs00820g.

54. J. Baronnier, J. Houel, C. Dujardin, F. Kulzer, and B. Mahler, "Doping $MAPbBr_3$ Hybrid Perovskites With CdSe/CdZnS Quantum Dots: From Emissive Thin Films to Hybrid Single-Photon Sources," *Nanoscale* 14, no. 15 (2022): 5769–5781, https://doi.org/10.1039/d1nr08473a.

55. S. Kim, "All-2D Material Photonic Devices," *Nanoscale Advances* 5, no. 2 (2023): 323–328, https://doi.org/10.1039/d2na00732k.

56. Y.-A. Chen, S. V. Naidu, Z. Luo, and C.-H. Chang, "Enhancing Optical Transmission of Multilayer Composites Using Interfacial

28359399, 0, Downloaded from https://onlinelibrary.wiley.com/doi/10.1002/ece2.70090 by Chung-Ang University, Wiley Online Library on [02/08/2026]. See the Terms and Conditions (https://onlinelibrary.wiley.com/terms-and-conditions) on Wiley Online Library for rules of use; OA articles are governed by the applicable Creative Commons License

Nanostructures," *Journal of Applied Physics* 126, no. 6 (2019): 063101, https://doi.org/10.1063/1.5097832.

57. F. Bouhjar, M. Mollar, M. Chourou, B. Marí, and B. Bessais, "Hydrothermal Synthesis of Nanostructured Cr-Doped Hematite With Enhanced Photoelectrochemical Activity," *Electrochimica Acta* 260 (2018): 838–846, https://doi.org/10.1016/j.electacta.2017.12.049.

58. K. Nakata and A. Fujishima, "TiO_2 Photocatalysis: Design and Applications," *Journal of Photochemistry and Photobiology C-Photochemistry Reviews* 13, no. 3 (2012): 169–189, https://doi.org/10.1016/j.jphotochemrev.2012.06.001.

59. A. R. Bhapkar and S. Bhame, "A Review on ZnO and its Modifications for Photocatalytic Degradation of Prominent Textile Effluents: Synthesis, Mechanisms, and Future Directions," *Journal of Environmental Chemical Engineering* 12, no. 3 (2024): 112553, https://doi.org/10.1016/j.jece.2024.112553.

60. L. Liao, M. Wang, Z. Li, X. Wang, and W. Zhou, "Recent Advances in Black TiO_2 Nanomaterials for Solar Energy Conversion," *Nanomaterials* 13, no. 3 (2023): 468, https://doi.org/10.3390/nano13030468.

61. H. Khan and M. U. H. Shah, "Modification Strategies of TiO_2 Based Photocatalysts for Enhanced Visible Light Activity and Energy Storage Ability: A Review," *Journal of Environmental Chemical Engineering* 11, no. 6 (2023): 111532, https://doi.org/10.1016/j.jece.2023.111532.

62. M. Liu, R. Zhao, F. Sun, et al., "Wavelength-Tuneable Near-Infrared Luminescence in Mixed Tin–Lead Halide Perovskites," *Frontiers in Chemistry* 10 (2022): 887983, https://doi.org/10.3389/fchem.2022.887983.

63. M. Anaya, G. Lozano, M. E. Calvo, and H. Míguez, "ABX_3 Perovskites for Tandem Solar Cells," *Joule* 1, no. 4 (2017): 769–793, https://doi.org/10.1016/j.joule.2017.09.017.

64. J. M. Frost, K. T. Butler, F. Brivio, C. H. Hendon, M. Van Schilfgaarde, and A. Walsh, "Atomistic Origins of High-Performance in Hybrid Halide Perovskite Solar Cells," *Nano Letters* 14, no. 5 (2014): 2584–2590, https://doi.org/10.1021/nl500390f.

65. J. Kim, S.-C. Lee, S.-H. Lee, and K.-H. Hong, "Importance of Orbital Interactions in Determining Electronic Band Structures of Organo-Lead Iodide," *Journal of Physical Chemistry C* 119, no. 9 (2015): 4627–4634, https://doi.org/10.1021/jp5126365.

66. Y. Liu, J.-P. Banon, K. Frohna, et al., "The Electronic Disorder Landscape of Mixed Halide Perovskites," *ACS Energy Letters* 8, no. 1 (2022): 250–258, https://doi.org/10.1021/acsenergylett.2c02352.

67. M. Pols, A. C. van Duin, S. Calero, S. Tao, and I. Mixing, "Br in Inorganic Perovskites: Atomistic Insights From Reactive Molecular Dynamics Simulations," *Journal of Physical Chemistry C* 128, no. 9 (2024): 4111–4118, https://doi.org/10.1021/acs.jpcc.4c00563.

68. R.-I. Biega, H. J. Jobsis, Z. Gijsberg, M. Huskens, E. M. Hutter, and L. Leppert, "Halide Mixing in $Cs_2AgBi(I_xBr_{1-x})_6$ Double Perovskites: A Pathway to Tunable Excitonic Properties," *Journal of Physical Chemistry C* 128, no. 35 (2024): 14767–14775, https://doi.org/10.1021/acs.jpcc.4c04453.

69. S. Hu, J. Thiesbrummel, J. Pascual, M. Stolterfoht, A. Wakamiya, and H. J. Snaith, "Narrow Bandgap Metal Halide Perovskites for All-Perovskite Tandem Photovoltaics," *Chemical Reviews* 124, no. 7 (2024): 4079–4123, https://doi.org/10.1021/acs.chemrev.3c00667.

70. H. Wang, A. Tal, T. Bischoff, P. Gono, and A. Pasquarello, "Accurate and Efficient Band-Gap Predictions for Metal Halide Perovskites at Finite Temperature," *npj Computational Materials* 8, no. 1 (2022): 237, https://doi.org/10.1038/s41524-022-00869-6.

71. K. O. Mastej, B. Batnaran, A.-P. M. Reponen, et al., "An Experimental Data Library for the Full $CsPb(Cl_xBr_{1-x})_3$ Compositional Series," *Chemical Communications* 61, no. 33 (2025): 6146–6149, https://doi.org/10.1039/d5cc00735f.

72. O. Stroyuk, O. Raievska, A. Barabash, et al., "Band-Bowing Effects in Lead-Free Double $Cs_2AgBi_xSb_{1-x}Cl_6$ Perovskites and Their Anion-Exchanged Derivatives," *Journal of Materials Chemistry C* 12 (2024): 533–544, https://doi.org/10.1039/d3tc04004f.

73. J. Lee, W. K. Chong, S. H. W. Kok, et al., "Mixed Halide Formation in Lead-Free Antimony-Based Halide Perovskite for Boosted CO_2 Photoreduction: Beyond Band Gap Tuning," *Advanced Functional Materials* 33, no. 42 (2023): 2303430, https://doi.org/10.1002/adfm.202303430.

74. J. Lee, E. Zhu, S. H. W. Kok, et al., "Bimetallic B-Site Halide Perovskites for Enhanced Photocatalytic CO_2 Reduction," *ACS Sustainable Chemistry & Engineering* 12, no. 36 (2024): 13427–13437, https://doi.org/10.1021/acssuschemeng.4c01348.

75. Z.-Y. Chen, N.-Y. Huang, and Q. Xu, "Metal Halide Perovskite Materials in Photocatalysis: Design Strategies and Applications," *Coordination Chemistry Reviews* 481 (2023): 215031, https://doi.org/10.1016/j.ccr.2023.215031.

76. S. H. Teo, C. H. Ng, Y. H. Ng, A. Islam, S. Hayase, and Y. H. Taufiq-Yap, "Resolve Deep-Rooted Challenges of Halide Perovskite for Sustainable Energy Development and Environmental Remediation," *Nano Energy* 99 (2022): 107401, https://doi.org/10.1016/j.nanoen.2022.107401.

77. A. H. Bhosale, S. Narra, S. S. Bhosale, and E. W.-G. Diau, "Interface-Enhanced Charge Recombination in the Heterojunction Between Perovskite Nanocrystals and BiOI Nanosheets Serves as an S-Scheme Photocatalyst for CO_2 Reduction," *Journal of Physical Chemistry Letters* 13, no. 34 (2022): 7987–7993, https://doi.org/10.1021/acs.jpclett.2c02153.

78. C. Liu, Y. Yang, H. Chen, et al., "Two-Dimensional Perovskitoids Enhance Stability in Perovskite Solar Cells," *Nature* 633, no. 8029 (2024): 359–364, https://doi.org/10.1038/s41586-024-07764-8.

79. X. Shen, X. Lin, Y. Peng, et al., "Two-Dimensional Materials for Highly Efficient and Stable Perovskite Solar Cells," *Nano-Micro Letters* 16, no. 1 (2024): 201, https://doi.org/10.1007/s40820-024-01417-1.

80. T. L. Leung, I. Ahmad, A. A. Syed, A. M. C. Ng, J. Popović, and A. B. Djurišić, "Stability of 2D and Quasi-2D Perovskite Materials and Devices," *Communications Materials* 3, no. 1 (2022): 63, https://doi.org/10.1038/s43246-022-00285-9.

81. Z. Fang, G. Wang, C. Guan, J. Zhang, and Q. Xiang, "Reducing Dielectric Confinement Effect Enhances Carrier Separation in Two-Dimensional Hybrid Perovskite Photocatalysts," *Angewandte Chemie International Edition* 63 (2024): e202411219, https://doi.org/10.1002/anie.202411219.

82. L. Zhang, C. Sun, T. He, et al., "High-Performance quasi-2D Perovskite Light-Emitting Diodes: From Materials to Devices," *Light: Science & Applications* 10, no. 1 (2021): 61, https://doi.org/10.1038/s41377-021-00501-0.

83. M. J. Rivera Medina, L. Di Mario, S. Kahmann, et al., "Tuning the Energy Transfer in Ruddlesden–Popper Perovskites Phases Through Isopropylammonium Addition—Towards Efficient Blue Emitters," *Nanoscale* 15, no. 14 (2023): 6673–6685, https://doi.org/10.1039/D3NR00087G.

84. C. C. Lin, J. Y. Li, N. Z. She, et al., "Stabilized High-Membered and Phase-Pure 2D all Inorganic Ruddlesden-Popper Halide Perovskites Nanocrystals as Photocatalysts for the CO_2 Reduction Reaction," *Small* 18, no. 19 (2022): e2107881, https://doi.org/10.1002/smll.202107881.

85. D. Wu, C. Tian, J. Zhou, et al., "Morphology and Structure of Lead-Free Cusb-Based Double Perovskites for Photocatalytic CO_2 Reduction," *Carbon Neutralization* 1, no. 3 (2022): 298–305, https://doi.org/10.1002/cnl2.30.

86. Z. Wang, M. Xiao, J. You, G. Liu, and L. Wang, "Defect Engineering in Photocatalysts and Photoelectrodes: From Small to Big," *Accounts of*

28359399, 0, Downloaded from https://onlinelibrary.wiley.com/doi/10.1002/ece2.70090 by Chung-Ang University, Wiley Online Library on [02/08/2026]. See the Terms and Conditions (https://onlinelibrary.wiley.com/terms-and-conditions) on Wiley Online Library for rules of use; OA articles are governed by the applicable Creative Commons License

Materials Research 3, no. 11 (2022): 1127–1136, https://doi.org/10.1021/accountsmr.1c00201.

87. Y. W. Liu, S. H. Guo, S. Q. You, et al., "Mn-doped $CsPb(Br/Cl)_3$ Mixed-Halide Perovskites for CO_2 Photoreduction," *Nanotechnology* 31, no. 21 (2020): 215605, https://doi.org/10.1088/1361-6528/ab72be.

88. S. Singh, D. Ganguly, S. Gupta, and V. Govind Rao, "Enhancing the Photocatalytic Performance of $CsPbBr_3$ Nanocrystals Through Ferrocene-Assisted Exciton Dissociation and Halide Vacancies," *ACS Applied Materials and Interfaces* 16, no. 49 (2024): 67854–67861, https://doi.org/10.1021/acsami.4c16781.

89. J. Pi, X. Jia, Z. Long, et al., "Surface and Defect Engineering Coupling of Halide Double Perovskite $Cs_2NaBiCl_6$ for Efficient CO_2 Photoreduction," *Advanced Energy Materials* 12, no. 43 (2022): 2202074, https://doi.org/10.1002/aenm.202202074.

90. Z. Fang, Z. Yu, M. Chen, and Q. Xiang, "Modulating Carrier Dynamics in Halide Perovskites Through Lattice Strain Engineering of $CsPb_{1-x}Cu_xBr_3$ for Improved Photocatalytic CO_2 Reduction," *ACS Nano* 19, no. 38 (2025): 34264–34272, https://doi.org/10.1021/acsnano.5c11198.

91. Q. Xu, L. Zhang, B. Cheng, J. Fan, and J. Yu, "S-Scheme Heterojunction Photocatalyst," *Chem* 6, no. 7 (2020): 1543–1559, https://doi.org/10.1016/j.chempr.2020.06.010.

92. G. Yin, X. Qi, Y. Chen, et al., "Constructing an all Zero-Dimensional $CsPbBr_3$/CdSe Heterojunction for Highly Efficient Photocatalytic CO_2 Reduction," *Journal of Materials Chemistry A* 10, no. 42 (2022): 22468–22476, https://doi.org/10.1039/D2TA05186A.

93. L. Li, Z. Zhang, C. Ding, and J. Xu, "Boosting Charge Separation and Photocatalytic CO_2 Reduction of $CsPbBr_3$ Perovskite Quantum Dots by Hybridizing With P3HT," *Chemical Engineering Journal* 419 (2021): 129543, https://doi.org/10.1016/j.cej.2021.129543.

94. Y. Wang, H. Huang, Z. Zhang, et al., "Lead-Free Perovskite $Cs_2AgBiBr_6$@g-C_3N_4 Z-scheme System for Improving CH_4 Production in Photocatalytic CO_2 Reduction," *Applied Catalysis B: Environmental* 282 (2021): 119570, https://doi.org/10.1016/j.apcatb.2020.119570.

95. L. Wang, J. Qiu, N. Wu, X. Yu, and X. An, "TiO_2/$CsPbBr_3$ S-Scheme Heterojunctions With Highly Improved CO_2 Photoreduction Activity Through Facet-Induced Fermi Level Modulation," *Journal of Colloid and Interface Science* 629 (2023): 206–214, https://doi.org/10.1016/j.jcis.2022.08.120.

96. Y. Wang, J. Hüpkes, S. Ravishankar, B. Klingebiel, and T. Kirchartz, "Loss Analysis of Halide-Perovskite Solar Cells Deposited on Textured Substrates," *Solar RRL* 9, no. 7 (2025): 2400829, https://doi.org/10.1002/solr.202400829.

97. N. O. Etafo, A. Okmi, S. Dey, H. Alzahrani, and A. Bamisaye, "Influence and Applications of Refractive Index on the Catalytic Perfomance of Photo-Responsive Materials," *Environmental Surfaces and Interfaces* 3 (2025): 237–264, https://doi.org/10.1016/j.esi.2025.09.004.

98. F. Wen and W. Liu, "Three-Dimensional Ordered Macroporous Materials for Photocatalysis: Design and Applications," *Journal of Materials Chemistry A* 9, no. 34 (2021): 18129–18147, https://doi.org/10.1039/D1TA04127D.

99. Z. Xu, F. Wang, L. Feng, and Y. Chen, "S-scheme Ag/ZnO/CeO_2 Inverse Opal Photonic Crystals With Enhanced Photocatalytic Properties," *Optical Materials* 139 (2023): 113770, https://doi.org/10.1016/j.optmat.2023.113770.

100. X. Deng, Q. Liang, J. Fan, et al., "Interface Engineering of Hollow $CsPbBr_3$/Co_3O_4 p-n Heterojunction With Rich Oxygen Vacancy for Highly Enhanced Photocatalytic CO_2 Reduction," *Chemical Engineering Journal* 475 (2023): 146385, https://doi.org/10.1016/j.cej.2023.146385.

101. Y.-F. Mu, J.-S. Zhao, L.-Y. Wu, et al., "Lead-Free Halide Perovskite Hollow Nanospheres to Boost Photocatalytic Activity for CO_2 Reduction," *Applied Catalysis B: Environmental* 338 (2023): 123024, https://doi.org/10.1016/j.apcatb.2023.123024.

102. Y.-X. Feng, K. Su, Z.-L. Liu, et al., "A Halide Perovskite Based Ternary Heterojunction With Multi-Shell Hollow Structure for Stable and Efficient Artificial Photosynthesis," *Applied Catalysis B: Environment and Energy* 347 (2024): 123821, https://doi.org/10.1016/j.apcatb.2024.123821.

103. X. Li, J. Liu, G. Jiang, X. Lin, J. Wang, and Z. Li, "Self-Supported $CsPbBr_3$/$Ti_3C_2T_x$ Mxene Aerogels Towards Efficient Photocatalytic CO_2 Reduction," *Journal of Colloid and Interface Science* 643 (2023): 174–182, https://doi.org/10.1016/j.jcis.2023.04.015.

104. B. N. Choi, J. Y. Seo, Z. An, P. J. Yoo, and C.-H. Chung, "An In-Situ Spectroscopic Study on the Photochemical CO_2 Reduction on $CsPbBr_3$ Perovskite Catalysts Embedded in a Porous Copper Scaffold," *Chemical Engineering Journal* 430 (2022): 132807, https://doi.org/10.1016/j.cej.2021.132807.

105. Z. Zhang, M. Shu, Y. Jiang, and J. Xu, "Fullerene Modified $CsPbBr_3$ Perovskite Nanocrystals for Efficient Charge Separation and Photocatalytic CO_2 Reduction," *Chemical Engineering Journal* 414 (2021): 128889, https://doi.org/10.1016/j.cej.2021.128889.

106. S. Zhao, Q. Liang, Z. Li, et al., "Layered Double Hydroxide Nanosheets Activate $CsPbBr_3$ Nanocrystals for Enhanced Photocatalytic CO_2 Reduction," *Nano Research* 15, no. 7 (2022): 5953–5961, https://doi.org/10.1007/s12274-022-4268-8.

107. I. Anghel and A. Petris, "Design of an all-Optical Tunable 2D Photonic Crystal in As_2S_3 Film," *Optics Communications* 574 (2025): 131247, https://doi.org/10.1016/j.optcom.2024.131247.

108. Y. Chen, L. Li, Q. Xu, et al., "Recent Advances in Opal/Inverted Opal Photonic Crystal Photocatalysts," *Solar RRL* 5, no. 6 (2021): 2000541, https://doi.org/10.1002/solr.202000541.

109. L. Han, Z. Dang, Y. Xi, L. Zhu, and S. Chen, "Carbon-Dots-Mediated Flexible Inverse Opal Perovskite Film Featuring Structural Robustness and Highly Selective Photocatalytic CO_2 Reduction," *Nano Research* 18, no. 11 (2025): 94907745, https://doi.org/10.26599/nr.2025.94907745.

110. X. Sun, K.-Y. Zhang, S.-Z. Zhou, and H.-H. Fu, "Robust Chirality-Induced Spin Selectivity in Topologically Chiral Molecular Knots," *Nature Communications* 17, no. 1 (2025): 1231, https://doi.org/10.1038/s41467-025-67988-8.

111. C. C. Lin, T. R. Liu, S. R. Lin, et al., "Spin-Polarized Photocatalytic CO_2 Reduction of Mn-Doped Perovskite Nanoplates," *Journal of the American Chemical Society* 144, no. 34 (2022): 15718–15726, https://doi.org/10.1021/jacs.2c06060.

112. C. C. Lin, S. K. Huang, W. N. Tseng, et al., "Chirality-Regulated Spin-Polarization of Perovskite Nanoplates for Photocatalytic CO_2 Reduction Reaction," *Journal of the American Chemical Society* 147, no. 44 (2025): 40347–40355, https://doi.org/10.1021/jacs.5c11357.

113. Z. Y. Pan, C. Z. Huang, L. Zhan, and J. Zhou, "Plasmonic Single Nanoparticle for Resonance Light Scattering Imaging Analysis and Applications," *TrAC, Trends in Analytical Chemistry* 164 (2023): 117090, https://doi.org/10.1016/j.trac.2023.117090.

114. Y. Zhu, H. Xu, P. Yu, and Z. Wang, "Engineering Plasmonic Hot Carrier Dynamics Toward Efficient Photodetection," *Applied Physics Reviews* 8, no. 2 (2021): 021305, https://doi.org/10.1063/5.0029050.

115. B. Ostovar, S. A. Lee, A. Mehmood, et al., "The Role of the Plasmon in Interfacial Charge Transfer," *Science Advances* 10, no. 27 (2024): eadp3353, https://doi.org/10.1126/sciadv.adp3353.

116. M. A. Alkhalayfeh, A. A. Aziz, M. Z. Pakhuruddin, and K. M. M. Katubi, "Recent Advances of Perovskite Solar Cells Embedded With Plasmonic Nanoparticles," *physica status solidi (a)* 218, no. 17 (2021): 2100310, https://doi.org/10.1002/pssa.202100310.

28359399, 0, Downloaded from https://onlinelibrary.wiley.com/doi/10.1002/ece2.70090 by Chung-Ang University, Wiley Online Library on [02/08/2026]. See the Terms and Conditions (https://onlinelibrary.wiley.com/terms-and-conditions) on Wiley Online Library for rules of use; OA articles are governed by the applicable Creative Commons License

117. R. Tang, H. Sun, Z. Zhang, et al., "Incorporating Plasmonic Au-Nanoparticles Into Three-Dimensionally Ordered Macroporous Perovskite Frameworks for Efficient Photocatalytic CO_2 Reduction," *Chemical Engineering Journal* 429 (2022): 132137, https://doi.org/10.1016/j.cej.2021.132137.

118. Y. Wu, X. Yue, J. Fan, X. Hao, and Q. Xiang, "In Situ Fabrication of Plasmonic Bi/$CsPbBr_3$ Composite Photocatalyst Toward Enhanced Photocatalytic CO_2 Reduction," *Applied Surface Science* 609 (2023): 155391, https://doi.org/10.1016/j.apsusc.2022.155391.

119. X. Wan, Y. Pan, Y. Xu, et al., "Ultralong Lifetime of Plasmon-Excited Electrons Realized in Nonepitaxial/Epitaxial Au@CdS/$CsPbBr_3$ Triple-Heteronanocrystals," *Advanced Materials* 35, no. 3 (2023): e2207555, https://doi.org/10.1002/adma.202207555.

120. J.-F. Liao, Y.-T. Cai, J.-Y. Li, et al., "Plasmonic $CsPbBr_3$–Au Nanocomposite for Excitation Wavelength Dependent Photocatalytic CO_2 Reduction," *Journal of Energy Chemistry* 53 (2021): 309–315, https://doi.org/10.1016/j.jechem.2020.04.017.

121. D. Li, R. Li, Y. Zhao, et al., "g-C_3N_4 as Ballistic Electron Transport "Tunnel" in $CsPbBr_3$-Based Ternary Photocatalyst for Gas Phase CO_2 Reduction," *Journal of Colloid and Interface Science* 666 (2024): 66–75, https://doi.org/10.1016/j.jcis.2024.03.193.

28359399, 0, Downloaded from https://onlinelibrary.wiley.com/doi/10.1002/ece2.70090 by Chung-Ang University, Wiley Online Library on [02/08/2026]. See the Terms and Conditions (https://onlinelibrary.wiley.com/terms-and-conditions) on Wiley Online Library for rules of use; OA articles are governed by the applicable Creative Commons License